Spring 5-15-2016

Improving Radiation Therapy Through Motion Tracking

Hanlin Wan
Washington University in St. Louis

Recommended Citation

Wan, Hanlin, "Improving Radiation Therapy Through Motion Tracking" (2016). *McKelvey School of Engineering Theses & Dissertations*. 152.
https://openscholarship.wustl.edu/eng_etds/152

WASHINGTON UNIVERSITY IN ST. LOUIS
School of Engineering and Applied Science
Department of Biomedical Engineering

Dissertation Examination Committee:
Parag Parikh, Chair
Mark Anastasio
Sasa Mutic
Robert Pless
Lihong Wang

Improving Radiation Therapy Through Motion Tracking

by

Hanlin Wan

A dissertation presented to the
Graduate School of Arts & Sciences
of Washington University in
partial fulfillment of the
requirements for the degree of
Doctor of Philosophy

May 2016

St. Louis, Missouri

Table of Contents

List of Figures

List of Tables

List of Abbreviations

95E2	percentage of data sets with a 95% error < 2 mm
CBCT	cone beam computed tomography
CT	computed tomography
DP	dynamic programming
DPTM	dynamic programming with template matching
DSC	Dice similarity coefficient
EBRT	external beam radiation therapy
FM	fiducial marker
IMRT	intensity modulated radiation therapy
ME1	percentage of data sets with a mean error < 1 mm
MHD	modified Hausdorff distance
mPTV	marker planned target volume
MR	magnetic resonance
MS	manual setup

PCA	principal component analysis
PTV	planned target volume
RPM	real-time position management
TM	template matching

Acknowledgments

First and foremost, I would like to express my sincere gratitude to my principal investigator, Dr. Parag Parikh, for his continuous support, guidance, and encouragement. He is not only a mentor for my studies and research, but also a mentor for life, teaching me valuable lessons for a future after graduation. I am especially grateful for his support and understanding with regard to my twin daughters, who were born during my studies. I cannot imagine being able to so successfully juggle family and work with a different mentor.

I would also like to extend my gratitude to my committee members, Drs. Mark Anastasio, Sasa Mutic, Lihong Wang, and Robert Pless, for their insightful comments and encouragement. In particular, Dr. Pless essentially acted as a second advisor, often meeting with me to discuss and guide my research. For that, I am truly thankful.

I would like to thank the Medical Physics group, in particular Leith Rankine, Austen Curcuru, and Dr. Lakshmi Santanam, as well as the radiation therapists, for their contributions to this research. Without their support and collaboration, I would have had no data on which to perform any of this research.

I had the great privilege of working with Dr. Per Poulsen and his group of students from Aarhus University, Denmark. Their inputs and contributions have been vital to the success of the presented work. I would also like to acknowledge all of the former and current members of our lab with whom I've had the pleasure of working. Not only are they great colleagues, but they are also incredible friends.

Last but not least, I would like to thank my family and friends for their continual support and encouragement. To my loving parents, who have supported all of my endeavors in life; to my father, who showed me what it means to never give up; to my daughters, who were my greatest source of inspiration; and to my wife, who has been there for me every step of the way with love, encouragement, and support: Thank You!

Hanlin Wan

Washington University in St. Louis
May 2016

ABSTRACT OF THE DISSERTATION

Improving Radiation Therapy Through Motion Tracking

by

Hanlin Wan

Doctor of Philosophy in Biomedical Engineering
Washington University in St. Louis, 2016
Parag Parikh, Chair

Radiation therapy is a widely-used cancer treatment method in which lethal doses of ionizing radiation are delivered to cancerous cells. Given the high dose requirements and the risk of associated complications, it is essential that radiation be targeted to cancerous cells while minimizing the dose to surrounding tissue. While current technology allows for accurate targeting of radiation dose, there is one major hurdle: Respiratory motion causes movement of up to a few centimeters of tumors in the abdomen and thorax, rendering even the most accurate radiation delivery machine highly inaccurate. Imaging devices integrated with the treatment machines allow us to visualize the moving tumors, either indirectly through x-ray imaging of nearby implanted fiducial markers, or directly through magnetic resonance imaging. The research presented here investigates two new methods of tracking the tumor motion on these modalities.

Chapter 1

Introduction

1.1 Respiratory Motion in Radiation Therapy

In radiation therapy, high doses of ionizing radiation are targeted at the cancerous tissue, causing damage to cell DNA that results in the shrinking or even complete recession of the tumor. Approximately 2/3 of all cancer patients will receive radiation therapy during their illness, with the majority receiving external beam radiation therapy (EBRT) [1]. In EBRT, large amounts of radiation are delivered through an external source. This radiation can originate from a variety of different sources, such as gamma rays from cobalt-60 machines or high-energy x-rays from linear accelerators. Because such high doses of radiation are required to kill tumor cells, it is important to direct as much of that radiation as possible to the cancerous tissues, while minimizing the dose to the surrounding, healthy tissue.

Today, intensity modulated radiation therapy (IMRT) [2] is by far the most common method of radiation delivery. In IMRT, each radiation beam is further divided into a number of smaller beamlets, all of which have their own intensity profiles (Figure

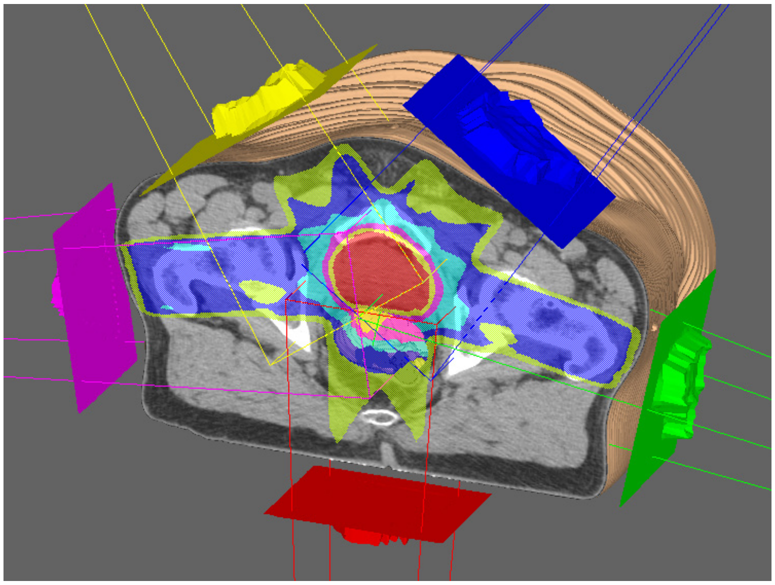

Figure 1.1: Schematic of an IMRT delivery. The radiation dose is highest in the targeted red portion in the middle and lower farther away from it.

1.1). Combined with the use of multiple beams directed from various angles, IMRT is able to deliver varying amounts of radiation to different tissues very precisely. This is especially important for organs that are particularly sensitive to radiation damage, such as the bowel, stomach, duodenum, or spinal cord, which may lie in close proximity to the targeted tumor volume.

The radiation therapy process consists of three steps. First, a patient simulation is performed, in which a volumetric image of the target anatomy is acquired. This is generally a computed tomography (CT) image, although the use of magnetic resonance (MR) images has been increasing in recent years. Second, the simulation images are imported into a treatment planning software, in which the radiation dose to the target is virtually planned, as in Figure 1.1. Finally, the patient is placed into the treatment machine for radiation dose delivery according to the treatment plan.

In the planning step, a computer algorithm optimizes the direction and profile of the beams based on physician-drawn contours and constraints. For example, the clinical target volume is the volume that encompasses the visible tumor and the unimageable tumor spread. This is the volume that must receive a high dose of radiation for optimal treatment. However, due to uncertainties in planning and delivery, the contour must be expanded into the planned target volume (PTV) to ensure that the entire tumor is irradiated. Other important contours include organs at risk, in which a maximum dose constraint is established in order to reduce damage to sensitive tissues.

In order to accurately deliver the radiation according to plan, the patient must be accurately set up on the treatment table, which is typically accomplished through the use of imaging with an integrated imager. The most common type of imager has an x-ray unit mounted 90° from the radiation delivery unit on the same rotating gantry. The data presented in Chapters 2 and 3 was acquired from such an imaging unit, namely the Varian Trilogy and TrueBeam machines (Varian Medical Systems, Palo Alto, CA). More recently, companies are looking to combine radiation delivery with an MR imager, allowing for significantly better soft tissue images without additional x-ray radiation to the patient. The data presented in Chapter 4 was acquired from the first integrated MR/radiation delivery machine to be used clinically, namely the ViewRay MRIdian (ViewRay Inc., Cleveland, OH) [3].

On each treatment day, or fraction, the patient undergoes imaging immediately prior to radiation delivery in order to ensure proper positioning on the treatment table. The radiation therapists then use these images to manually line up the physician-assigned targets on the pre-treatment image to the planning image. In patients with thoracic or abdominal tumors, there is the added challenge of respiratory motion, which can result in tumor movement up to several centimeters. If not taken into account, this motion causes reduced dose to the target cells and an increased dose to the surrounding, healthy tissue [4, 5].

There are multiple ways in which physicians can account for respiratory motion. The most commonly used method is a motion-encompassing technique. By using imaging such as slow CT [6] or four-dimensional CT [7], physicians can estimate the extent of the tumor motion as well as establish a time-averaged tumor location. By planning the radiation based on this mean position and taking into account the magnitude of the motion, the expected dose blurring effect of respiration can be compensated [8].

Another method is respiratory gating, in which the radiation dose is delivered only when the patient is in a certain phase of the respiratory cycle. To perform respiratory gating, the motion of the target needs to be tracked through the use of respiratory surrogates, typically a combination of internal and external surrogates. The motion of the internal surrogate, typically a fiducial marker (FM) implanted in close proximity to the tumors, is correlated with an easily tracked external surrogate, such as Varian's Real-time Position Management (RPM) system (Varian Medical Systems, Seattle, WA). The radiation beam is then gated on or off depending on set boundaries for the values obtained from the external surrogate. In the case of ViewRay's MR system, gating can be performed directly on the tumor itself as seen on the MR images.

In order to effectively apply motion management, it is essential to track the tumor motion accurately. The research here addresses such tracking issues. Chapters 2 and 3 investigate the tracking of FMs in fluoroscopic and cone beam CT (CBCT) images, respectively, while Chapter 4 investigates the tracking of the tumors directly in MR images.

1.2 Fiducial Tracking in X-Ray Images

FMs are commonly used in EBRT to aid in the patient setup. Since the tumors are not usually visible with x-ray imaging, FMs are implanted near the tumor as surrogates. The FMs can then be used to align the patient to the FMs from the planning CT. Because of nonridity of the internal organs, the use of FMs can greatly increase the setup accuracy compared to aligning the patient using skin marks [9, 10] or bony anatomy [11, 12].

To set up a patient using FMs, x-ray images are acquired immediately prior to treatment, and the FMs are then manually aligned to those in the planning CT. This is usually in the form of a pair of orthogonal fluoroscopy images and/or a CBCT image. For a stationary target, two images acquired 90° apart is sufficient to accurately localize the marker in 3D space. However, for a moving target, a CBCT acquisition is preferred. A CBCT image is a series of hundreds of fluoroscopic images acquired at different gantry angles over the course of about a minute. These images can then be reconstructed into a 3D volume for marker alignment.

Due to respiratory motion and the long acquisition time for CBCT, the reconstructed volume will have a marker that is blurred in the superior-inferior direction. A good strategy for patient setup is to align the time-averaged, mean marker position to the marker in the planning CT. This theoretically results in a perfect alignment with the average marker location and therefore the highest planned dose will be in the same location. Another strategy is to use respiratory gating, in which the beam is turned on and off based on the FM location. The beam would be on only when the marker is within the contoured boundary, which we will call the marker PTV (mPTV). Respiratory gating allows for a smaller range of motion in which the beam is on, therefore reducing the dose blurring effect. Setting up the patient using the mean marker position can be time consuming and inaccurate due to the blurred images, and using respiratory gating is even more time consuming to set up. Chapters 2 and 3 attempt to address this issue by tracking the motion of the FMs in these x-ray images and automatically optimizing the patient setup for both the mean marker position setup as well as the gating setup.

1.3 Tumor Tracking in Cine MR Images

While FMs are the current gold standard for tumor localization, there are some drawbacks to their use. FM implantation is an invasive procedure; there are restrictions on where the FMs can be implanted; FMs may migrate over time; and tumors can shrink, grow, and deform in ways such that FMs cannot accurately describe their locations [13]. One solution is to use MR imaging to image the tumors directly rather than rely on a FM surrogate.

Combining MR imaging with radiation delivery is a difficult problem due to interference of the strong magnetic field with the radiation delivered to the patient [14]. ViewRay tackled this problem by using a weaker 0.35 T magnet combined with three gamma-emitting cobalt-60 sources. This combination has been shown to produce plans comparable to those from traditional linear accelerators [15–17].

With MR imaging of the tumor during treatment, respiratory gating can be performed directly on the tumor target as opposed to on FMs. Similar to the mPTV concept, where the FM must stay within a specified contour, gating on the ViewRay can be performed with a physician-specified contour for the tumor motion. The tumor target would be automatically tracked and the beam would be turned off when it leaves the specified boundaries. However, the current clinical tracking software on the ViewRay is not very robust, making gating less than optimal. Traditional tracking algorithms also do not work well due to the poor image contrast and resolution as a result of the weak magnetic field. Chapter 4 attempts to address the tracking of the tumor in a new, more robust way.

Chapter 2

Fiducial Tracking in Fluoroscopic Images[†]

Fluoroscopic images can be acquired using an onboard imager both prior to and during treatment. Although this process allows the physician to visualize FM motion and make decisions on how best to manage it, it is impractical for the physician to monitor the entire duration of treatment. Previous works have attempted to address this issue by automating the tracking of FMs. In this chapter, we present a new method for tracking FM in fluoroscopic images and compare it to previous, template based methods.

[†] The work in this chapter has been previously published in [18]. © Institute of Physics and Engineering in Medicine. Reproduced with permission. All rights reserved.

2.1 Background and Significance

Knowledge of a moving tumor's location is critical for optimal radiation delivery [19], as it allows for better selection of gating windows [20,21] and determination of the actual dose prescribed to the patient [22,23]. One way to track this tumor motion is by tracking the nearby implanted FMs seen through x-ray imaging.

A number of different groups has worked on algorithms to track FMs in fluoroscopic images. Nederveen et al. used a marker extraction kernel as the template for cylindrical FMs [24–26]; Shirato et al. modeled gold spheres by creating templates with 2D Gaussian distributions [27]; and Tang et al. used rectangular templates to model gold spherical and cylindrical FMs [28]. Each of these algorithms required prior knowledge of the exact shape and size of the FMs. A different algorithm, created by Balter et al., did not require specific known marker shapes and instead a reference image as the template [29,30]. These algorithms are all based on template matching (TM) and its derivatives, with specific requirements for the marker shape (generally spherical or cylindrical) and size, as well as for images with good contrast and no background clutter.

These algorithms generally work well with FMs that have known, regular shapes and high signal-to-noise ratios. However, multiple companies are now developing coiled FMs (e.g. Visicoil - RadioMed Corp., Bartlett, TN; VortX - Boston Scientific Corp., Natick, MA), which are smaller in size and irregular in shape, making them both easier to implant and less likely to migrate [31,32]. Coiled FMs appear in images with irregular shapes as well as lower contrast and signal-to-noise ratios. As a result, they require a reference image approach to TM, in which the user must manually create the template. As will be demonstrated later in this chapter, the performance of TM algorithms with this approach greatly depends on the quality of the template.

We present here a novel method based on an optimization algorithm known as dynamic programming (DP) that can robustly track implanted FMs of any size, shape, or orientation in fluoroscopic images. The first paper on DP was published in 1952 [33], and since then, this method has been used for numerous optimization problems in many different fields. We will show that for tracking FMs in fluoroscopic images, our DP-based algorithm greatly outperforms the current TM based methods.

2.2 Materials and Methods

2.2.1 Tracking Algorithm

The FM tracking algorithm is a 2-step, iterative method that alternates between constraining the search window and running the DP optimization. The search window is used to limit the search space for the FM in image i to a 100×100 box (approximately 23×23 mm) centered at

$$\begin{aligned} P_u(i) &= p_u \\ P_v(i) &= p_v + s \cdot RPM_i \, . \end{aligned} \tag{2.1}$$

s is the scaling factor for the respiratory surrogate signal value RPM, and (p_u, p_v) is the expected coordinate of the marker in the absence of motion. For the first iteration, p_u and p_v is manually selected and $s = 0$.

The 23 mm search window roughly corresponded to the maximum range of the FMs in 95% of data sets. The use of a search window decreases the computational complexity while increasing the robustness of the algorithm. The FM does not typically move much laterally in the u direction, hence the constant $P_u(i)$. However, due to respiratory motion, it can deviate substantially in the v direction. Therefore, $P_v(i)$ has an adjustment term that correlates to an external respiratory surrogate.

The second step is the DP step, in which a cost function $f(p_1, p_2, \ldots, p_N)$ is minimized. Each p_i is a vector of all the possible FM locations in image i, and N is the number of images. In the fluoroscopic images, radiopaque FMs have a lower intensity than neighboring pixels. Therefore, the list of possible locations corresponds to all of the local minima in the search window. Smoothing with a Gaussian kernel ($\sigma = 7$ pixels) removes much of the noise without eliminating the minima associated with the actual FMs, reducing the number of local minima to about 50 per search window.

The DP optimization algorithm is used to find the (u_i, v_i) in each p_i such that the following cost function is minimized:

$$f(p_1, p_2, \ldots, p_N) = \sum_{i=1}^{N} g(p_i) + \alpha \sum_{i=1}^{N} h(p_i) + \beta \sum_{i=1}^{N-1} k(p_i, p_{i+1}) \tag{2.2}$$

where

$$\begin{aligned} g(p_i) &= \sqrt{(u_i - c_{u,i})^2 + (v_i - c_{v,i})^2} \\ h(p_i) &= I(u_i, v_i) \\ k(p_i, p_{i+1}) &= \sqrt{(u_i - u_{i+1})^2 + (v_i - v_{i+1})^2}\,. \end{aligned} \tag{2.3}$$

$g(\cdot)$ and $h(\cdot)$ are cost functions that depend only on image i while $k(\cdot)$ is a cost function that depends on two neighboring images, i and $i+1$.

$g\left(p_i\right)$ is the Euclidean distance from the center of the search window $\left(c_{u,i}, c_{v,i}\right) = \left(P_u\left(i\right), P_v\left(i\right)\right)$ to the minima $\left(u_i, v_i\right)$. This term forces the minimum cost to occur when the FM is close to the center of the search window. $k\left(p_i, p_{i+1}\right)$ is the Euclidean distance between possible minima in adjacent images. Since images are acquired at 11 Hz, it is assumed that the FM does not move much between successive images. Therefore, this term forces the minimum cost to occur when the FM moves the least between successive images. $h\left(p_i\right)$ is the linearly rescaled grayscale intensity value I such that the extreme values for the pixels in each p_i are 0 and 1. FMs have lower intensities than the background, and therefore, this term forces the minimum cost to occur at the lowest intensity pixel. The parameters, $\alpha = 35$ and $\beta = 10$, were determined empirically to balance the need to constrain motion between images with the need to avoid false minima.

After the DP step, the algorithm returns to step 1 with a refined search window (new p_u, p_v, and s) such that the sum of distances between the set of $\left(P_u, P_v\right)$ and the set of DP-tracked location $\left(u_i, v_i\right)$ over all of the images is minimized:

$$f\left(p_u, p_v, s\right) = \sum_{i=1}^{N} \sqrt{\left(p_u - u_i\right)^2 + \left(p_v + s \cdot RPM_i - v_i\right)^2}\,. \tag{2.4}$$

The algorithm alternates between optimizing $\left(u_i, v_i\right)$ by minimizing Equation 2.2 and optimizing p_u, p_v, and s by minimizing Equation 2.4 until less than 1% of the predicted locations change between iterations. In general, 2-3 iterations are required for convergence.

After convergence, the set of $\left(u_i, v_i\right)$ for each fluoroscopy image i from the final iter-

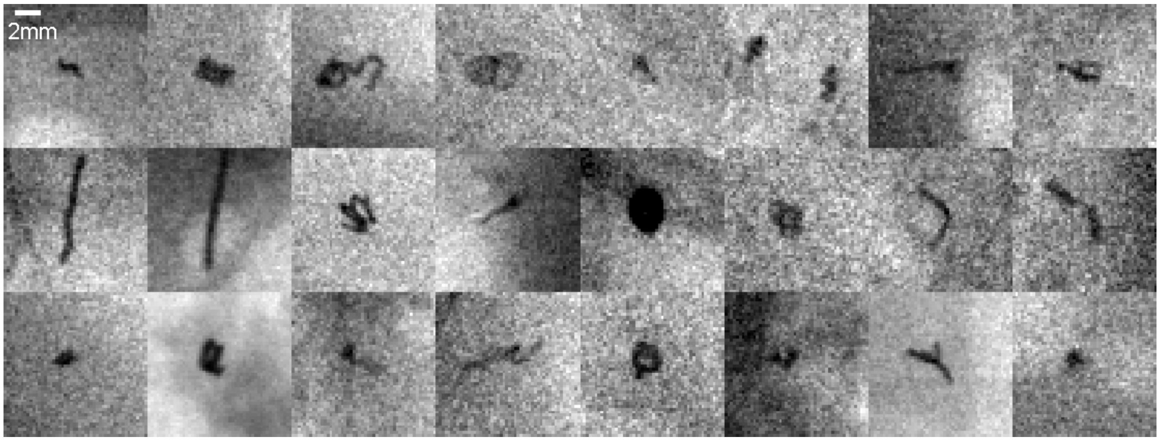

Figure 2.1: Sample FMs from each of the 24 patients.

ation is used in conjunction with TM (normalized cross correlation) to further refine the tracking, resulting in the DPTM algorithm. Unlike previous TM algorithms, the location of the FM is already known, and therefore, the search space for TM only needs to be twice the size of the template in each direction. This small search window prevents failed tracking due to nearby objects and drastically improves robustness.

For data sets with multiple FMs, the tracking is performed on each FM individually, independent of the other FMs.

2.2.2 Test Data

To test the DPTM algorithm and to compare it with previous TM algorithms, fluoroscopy images were collected from 24 different patients (14 liver, 7 pancreas, 3 lung) over multiple fractions, resulting in a total of 407 data sets. Each data set contained about 225 images. The range of motion for each FM is 12 ± 5 mm, with the largest motion being 30.7 mm. Figure 2.1 shows examples of FMs (all Visicoil) from each of the 24 patients. It is clear that the FMs have a wide range of shapes and sizes.

To establish a ground truth, a bounding box was manually drawn around the FMs in each image for each data set. The true location of the FM is then taken to be the center of the box. The accuracy of manual contouring is estimated to be better than 2 pixels (0.5 mm). These true locations are then used to evaluate the performance of the different algorithms based on two metrics: mean error and 95% error. The mean error is the mean distance from the true locations to the outputted locations across all the images in a data set. This gives an idea of the overall performance of the algorithm. The 95% error is the distance from the true to the outputted locations that 95% of the images in a data set fall below. This gives an idea of the consistency of the algorithm, which is very important in clinical settings.

Since TM algorithms are very sensitive to the template used, each data set was tested with three different templates. Figure 2.2 on the left shows a 100×100 pixel (23×23 mm) search window for one of the images. The search window in each image was always centered at the true location to simulate a best-case scenario. On the right are the three templates used. The top template comes from manually outlining the FM in the first image of the data set (contoured template). For each data set, 10 random images were chosen to create the other two templates. These were created by cropping the image around the known true location. The size of template used was the same as the contoured template with a 7-pixel (1.6 mm) padding added on all four sides. After 10 such trials, the templates that resulted in the lowest and highest mean errors (corresponding to the best and worst templates in Figure 2.2) were saved and used for all further comparisons. For this patient, the FM rotated during respiratory motion. The best and worst templates corresponded to different orientations of the FM.

For each data set, the FM locations were also tracked using our DP algorithm with no

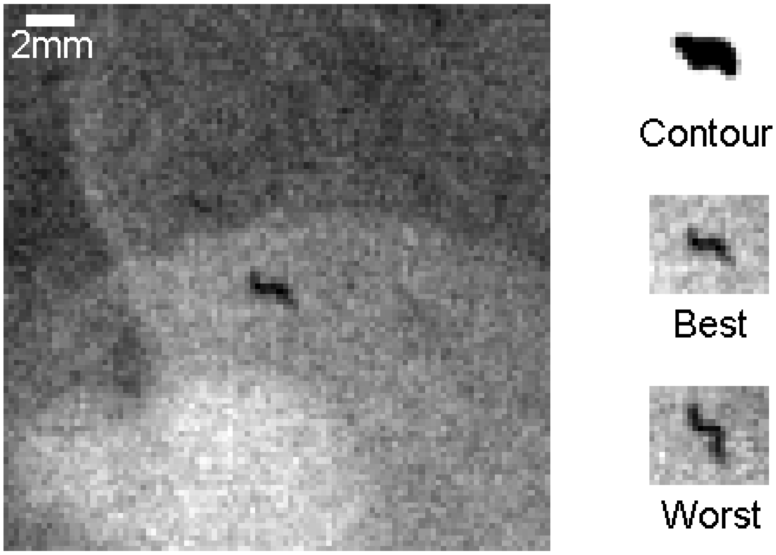

Figure 2.2: Images for Patient #1. Left: One example of a 23×23 mm search space. Right: The 3 templates used for testing; contour - manually traced outline, best - template resulting in best tracking performance with TM, worst - template resulting in worst tracking performance with TM.

TM refinement, as well as with the same three templates as used in TM (DPTM). All instances of TM use the normalized cross correlation between the template and the search space to find the pixel corresponding to the greatest correlation.

In the rest of this chapter, we first explore the performance of TM using various templates. Next, we compare DP, which does not require a user-defined template, to TM using the best possible template. Finally, we show the tracking accuracy by using DPTM.

2.3 Results

Figure 2.3 shows the tracking results for the same data set as shown in Figure 2.2 using the three different templates for TM as described in Section 2.2.2. The images

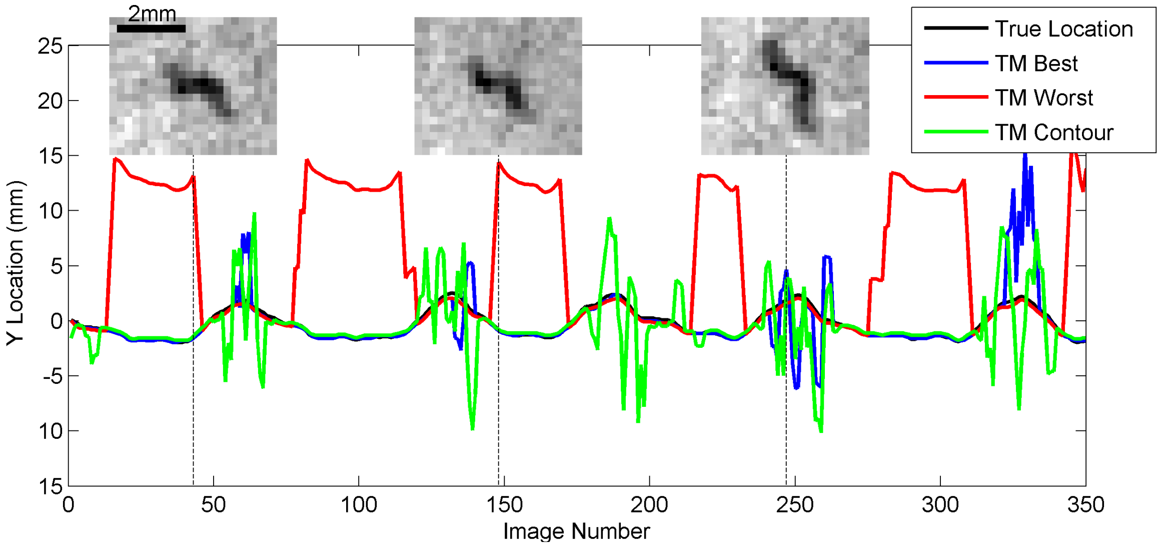

Figure 2.3: Tracking results comparing TM using the best, worst, and contoured templates on the same data set as used in Figure 2.2. The images on the vertical dashed lines represent the corresponding actual image of the FM. The errors are caused by differences in the FM orientations at different breathing phases coupled with the different orientations of the 3 templates.

at the top are the corresponding actual images of the FM at that time. The two on the left show the FM in a horizontal orientation. In these situations, TM best and TM contour, whose templates had the same horizontal orientation, accurately located the FM. On the other hand, the TM worst template, which had a vertical orientation, failed in these images. Instead, it located a second FM which was oriented vertically and located about 15 mm away. The rightmost image corresponded to peak inhalation, where the FM rotated to a vertical orientation. In these images, TM best and TM contour matched to random background objects, while TM worst accurately located the FM.

Table 2.1 summarizes the performance of TM on the 407 data sets with the different templates. For conciseness, the metric ME1 will be defined as the percentage of data sets with a mean error of 1 mm or less, and the metric 95E2 will be defined as the

Table 2.1: Comparison of the ME1 and 95E2 for DP, TM, and DPTM with the 3 different templates on 407 data sets. ME1 - percentage of data sets with a mean error of 1 mm or less; 95E2 - percentage of data sets with a 95% error of 2 mm or less.

Algorithm	**ME1**	**95E2**
TM Best	92.4	88.2
TM Worst	71.7	66.8
TM Contour	47.4	42.5
DP	90.7	90.2
DPTM Best	99.3	98.3
DPTM Worst	98.5	98.0
DPTM Contour	99.0	98.8

percentage of data sets with a 95% error of 2 mm or less. The best template performed very well, with an ME1 of 92% and 95E2 of 88%. However, the worst and contoured templates performed much worse, further demonstrating the importance of choosing a good template for TM.

Figure 2.4 shows the tracking results using DP on the same data set as used in Figures 2.2 and 2.3. In this example, the locations outputted by the DP algorithm is much more accurate than any of the TM algorithms. The only necessary input for DP is an approximate starting location so that the algorithm knows where to start searching for the FM.

Table 2.1 shows that over the 407 data sets, DP performs as well as TM best, with a ME1 of 91% and a 95E2 of 90%.

Because DP uses local minima to determine possible FM locations, and has no a-priori information on where these minima fall along the overall shape of the FM, it may not necessarily always pick the same location on the FM in all the images. Figure 2.5 is a good example of this. The FM is approximately 10 mm long, and the estimated FM location by DP fluctuates wildly. The DP algorithm is based on the assumption that

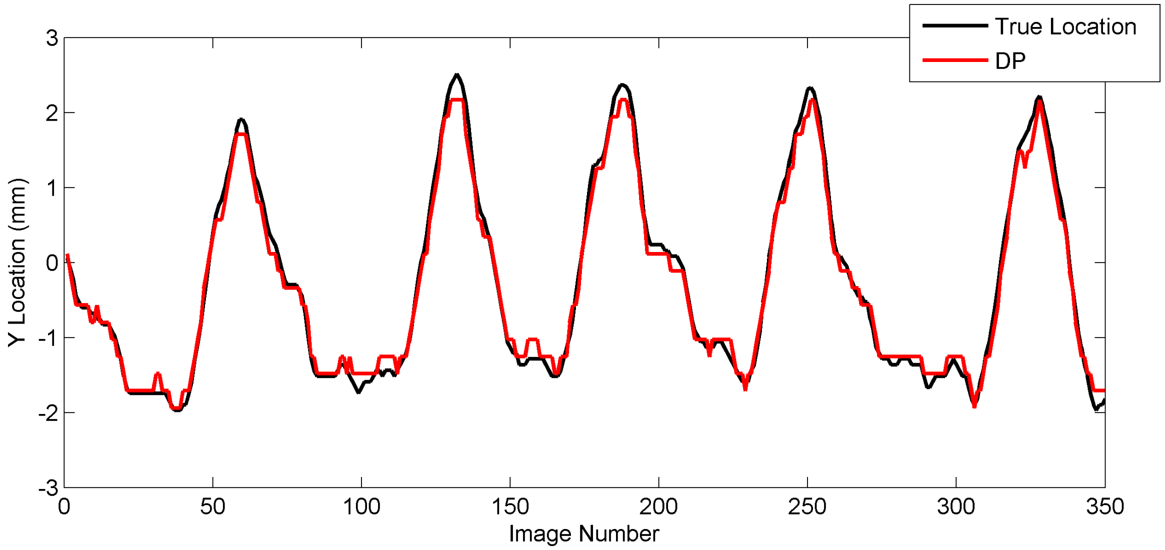

Figure 2.4: Tracking results using DP on the same data set as used in Figures 2.2 and 2.3.

the images are acquired at a fast enough rate that the FMs do not move much between successive images. Since the possible FM locations correspond to local minima in the images, and large FMs are likely to contain multiple local minima, the DP algorithm will choose the points on the FM that results in the least movement. While the figure shows that DP appears to have failed to properly track the FM, visual inspection revealed that the estimated location was in fact somewhere on the FM in every single image.

Figure 2.6 plots the mean and 95% errors of DP as a function of FM size. The size of the FM was defined as the diagonal length of the bounding box from the contoured templates. It appears that the error of the DP algorithm does indeed increase as the size of the FM increases.

To track larger FMs more accurately, a TM refinement step was added after DP (DPTM). Since DP does very well at locating some point on the FM, the template used for the TM step can be very small, and the search space only needs to be twice

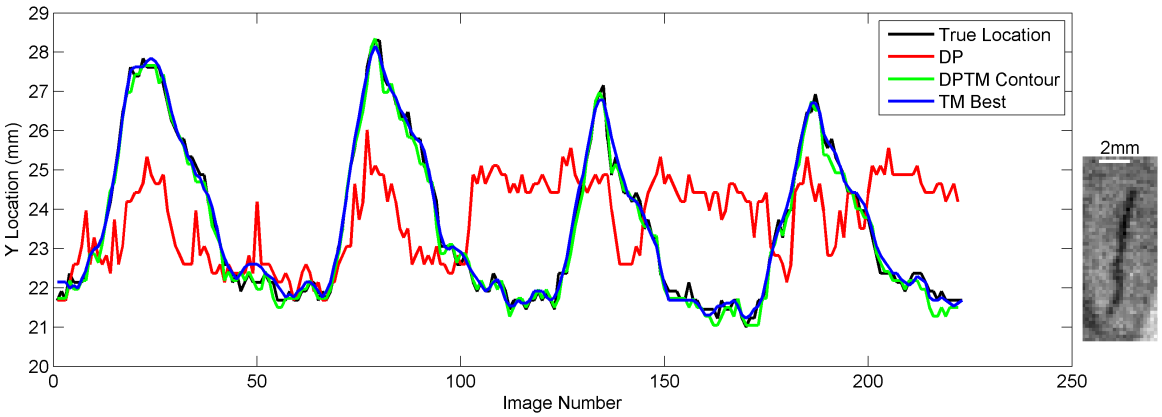

Figure 2.5: Tracking results comparing DP, DPTM contour, and TM best on Patient 2. While DP appears to fail to properly track the FM, the estimated location is on the FM in every image. An image of the FM is shown on the right.

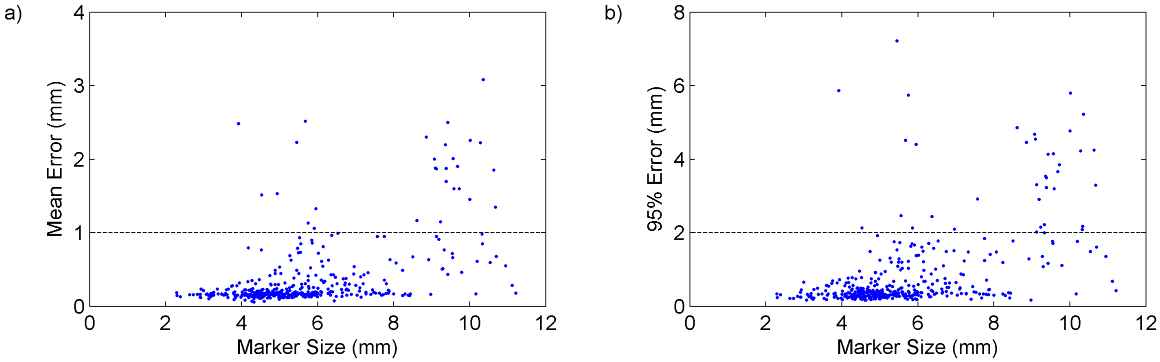

Figure 2.6: **(a)** Mean and **(b)** 95% error for DP with no template as a function of the FM size, defined as the diagonal length of the bounding box from the contoured templates.

the size of the template in each direction. Not only does this smaller search window decrease the computation complexity of TM, but it also makes TM much more robust to background noise and other objects. Figure 2.5 shows that the tracked FM locations using DPTM with the contoured template is very accurate, despite the DP location fluctuating wildly over the long FM.

Table 2.1 shows that the template used for DPTM does not affect its performance, Regardless of whether it is the contoured, best, or worst template, DPTM was able to achieve an ME1 of about 99% and 95E2 of 98%, which are far better than TM best (ME1 = 92%, 95E2 = 88%). This shows that DPTM can improve on the performance of TM without worrying too much about the quality of the template.

2.4 Discussion

In this chapter, we have presented a new algorithm, DPTM, to track any FM in fluoroscopic images. Previous algorithms used to track FMs are all based on TM or derivatives thereof [24–30]. These algorithms have strict requirements on template generation in order to achieve optimal results. Furthermore, these algorithms were mostly tested on gold spheres or cylinders. However, physicians are moving more towards flexible, coiled FMs, which can take on any arbitrary shape in the acquired images. We showed in Figure 2.3 and Table 2.1 that the performance of these TM based methods varies greatly depending on the quality of the templates. We showed that when a good template is used, TM is fairly robust. However, when the template is suboptimal, TM may often stray from the true FM locations, and track to background objects. In clinical settings, the physicians may not have the luxury of creating and testing multiple templates to see which one performs the best.

Figure 2.4 shows that DP performs much better than all three TM cases on this particular data set. DP by itself does not require the user to create an initial template; the user only has to input a single approximate point for each FM. This input can come from the FM locations contoured in the pre-planning CT images, as will be demonstrated in Chapter 3 on tracking FMs in CBCT images. This would make the algorithm fully automatic, requiring no additional user inputs. The iterative nature and global optimization of the DP algorithm allows for more accurate tracking as long as the initial point is close, making the algorithm much more robust to variances in initialization.

Figures 2.5 and 2.6 reveal a major drawback of DP. It does not perform as well with FMs larger than 7-8 mm. The DP algorithm uses local minima information from the images to determine possible FM locations. On large FMs, there may exist multiple local minima. Since the algorithm attempts to minimize the motion of the FMs from image to image, the tracked locations from DP are likely to jump around on the actual FM. In Figure 2.5, DP appears to completely fail to track the FM. However, on visual inspection, the output location in every image did indeed correspond to a point on the FM, but that point did not stay at a consistent location. Figure 2.6 shows that with the exception of a few outliers, FMs smaller than 7-8 mm can be accurately tracked using the DP algorithm alone.

In order to address the issue of large FMs, the DPTM variation was introduced, which adds a TM step after DP. Since DP is able to accurately locate the FM, the additional TM step requires a search window that is only twice the size of the template in each direction. This small search window makes the TM step much more robust to inter-

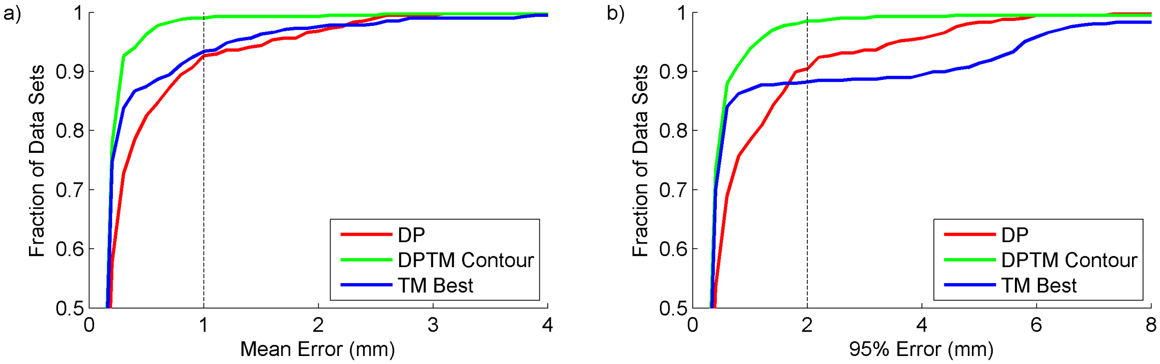

Figure 2.7: Tracking statistics for the 407 data sets. **(a)** Mean and **(b)** 95% error comparing TM best, DPTM contour, and DP with no template.

ference from background objects. Table 2.1 shows that the template used has very little effect on the performance of DPTM, unlike in TM alone. This template information can be extracted from the contours in the pre-planning CT images, making DPTM also fully automatic. Furthermore, the additional TM step greatly improves the tracking accuracy, especially for larger FMs. Figure 2.5 shows an example where DPTM was able to improve on the performance of DP when tracking large FMs.

Figure 2.7 shows a more detailed analysis of the results comparing TM best, DP, and DPTM contour. It clearly shows DPTM as the best performer even when using the template that performed the worst with TM and DP performing on par with TM best, without the use of any templates. Figure 2.8 shows the 95% error for each data set, sorted by patient. For 12 of the 24 patients, both TM and DPTM had 95% errors less than 2 mm for all data sets. However, for the remaining patients, TM had much more variation in performance than DPTM. The DPTM 95% error was greater than 2 mm in only 5 out of the 407 cases compared to 48 of the TM data sets. This shows that DPTM is much more robust than even TM in the best case scenario.

A major assumption used by the DP algorithm is that the images are acquired quickly enough that the FMs do not move much between successive images. To test the effect

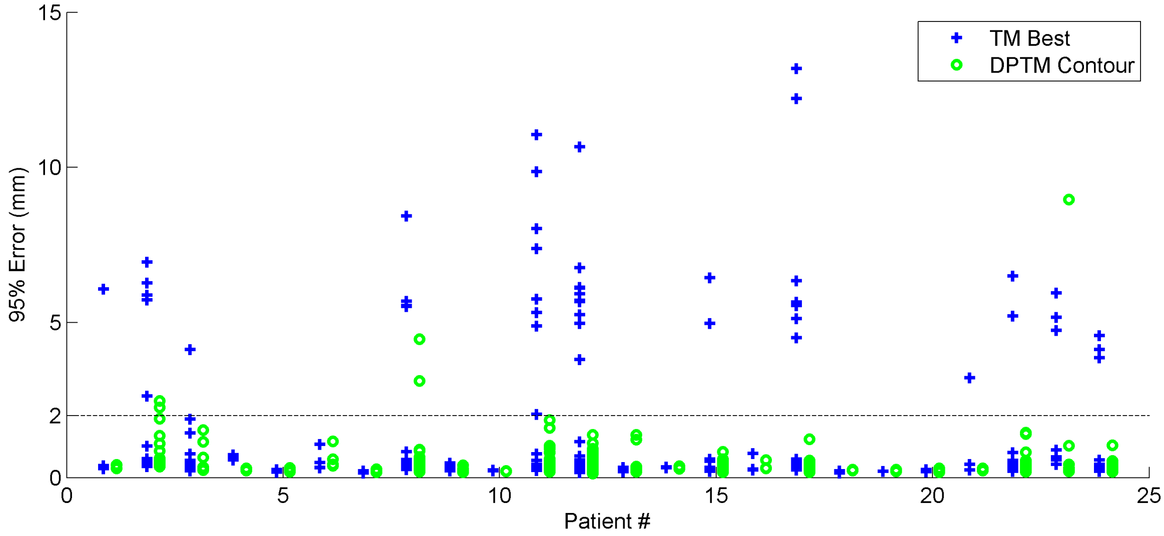

Figure 2.8: 95% error for each data set for each patient. 402/407 (98.8%) of DPTM contour data sets had 95% error < 2 mm, compared to 359/407 (88.2%) of TM data sets.

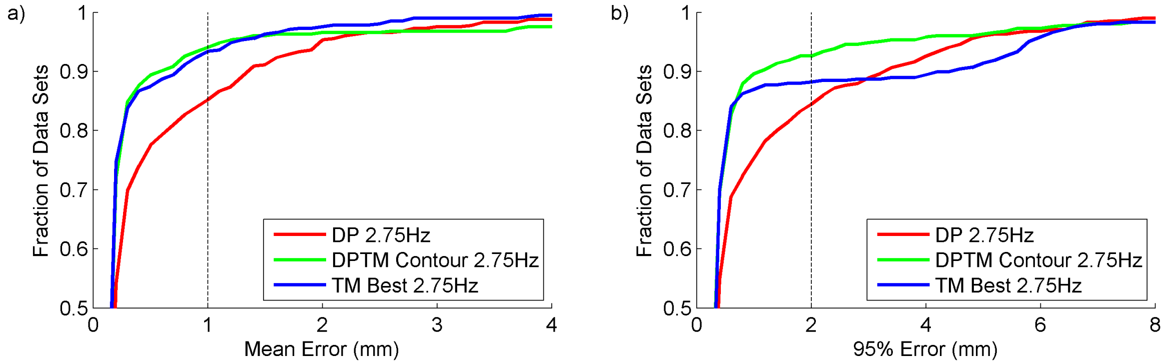

Figure 2.9: Tracking statistics for the 407 data sets. **(a)** Mean and **(b)** 95% error comparing TM best, DPTM contour at 2.75 Hz, and DP at 2.75 Hz.

of different temporal frequencies with which the images are acquired, the DP algorithm was run on every nth image to simulate various imaging frequencies. Images acquired at 2.75 Hz (using every 4th image) still perform very well, as can be seen in Figure 2.9, which shows the mean and 95% error comparing TM, DP, and DPTM at 2.75 Hz. Since TM does not use information from neighboring images, its performance remains unchanged. The performance of DP and DPTM both decrease as the imaging frequency decreases. However, at 2.75 Hz, the ME1 and 95E2 are both higher for DPTM (94% and 93%) than for TM best (93% and 88%). This shows that DPTM can still be used for fluoroscopy images acquired at a relative low frequency.

In conclusion, we showed that for tracking FMs in fluoroscopic images, DP alone works as well as the traditional TM algorithms without needing any information about the shape or size of the FMs. Furthermore, by combining TM with DP, DPTM was able to greatly improve the tracking accuracy, even when using the contoured templates where TM performed very poorly.

Chapter 3

Fiducial Tracking in CBCT Images[†]

CBCT images are typically acquired right before treatment to aid in patient setup. However, this is a manual and very time consuming process. In this chapter, we extend the DP tracking algorithm to automatically track FMs in CBCT images. We then use these tracked locations to automatically optimize the patient setup using two different techniques at two different institutions. Finally, we compare the accuracy and duty cycle of our DP-optimized setup to the actual setup used clinically for treatment.

[†] The work in this chapter has been previously published in [34]. ⓒ Institute of Physics and Engineering in Medicine. Reproduced with permission. All rights reserved.

3.1 Background and Significance

In order to properly position thoracic and abdominal patients, a CBCT is acquired prior to treatment and reconstructed into a 3D volume for registration with the planning CT. The registration process, which is manually performed by the therapists, is very time-intensive and potentially suboptimal due to blurring of the FMs caused by respiratory motion during the minute-long CBCT acquisition. To automate this patient setup, the FMs must first be accurately tracked in the CBCT projections.

Unlike the FMs tracked in fluoroscopic images in Chapter 2, FMs in CBCT images appear as different shapes and orientations depending on the gantry angles. This makes tracking FMs in CBCT images more difficult, especially when using a template based method. As a result, previous TM based methods require prior knowledge of the FM shape [28, 35–41]. Most require that the shape be either spherical or cylindrical, and user intervention is often necessary to select the FM in the first frame or to aid in creating a 3D model. These restrictions make clinical implementation difficult. Here, we extend our DP algorithm to track arbitrarily shaped FMs in CBCT projections with no user intervention.

By fully automating the FM tracking process, we can then automatically calculate the optimal patient couch position, such as one based on the mean marker position [42, 43]. For gated patients, there are two additional parameters that need to be optimized in addition to the couch position: the upper and lower gating bounds [44]. This added complexity makes the clinical cost of gating nontrivial, and as a result, not as widespread. The major challenges of daily gating include increased patient setup time due to additional imaging and operator selection of gating window as well as the clinical cost of training the physicians/therapists to decide on the gating window. In this work, we further developed an automated method to optimize both the patient couch position and the gating bounds using the FM locations as obtained using the DP algorithm.

Finally, we use intrafraction images acquired every 3 seconds during therapy as the ground truth for the FM location during treatment in order to compare the DP-optimized patient setup to the current clinical setup at two different institutions.

3.2 Materials and Methods

3.2.1 Tracking Algorithm

In Section 2.2.1, we described the DP algorithm as applied to tracking FMs in fluoroscopic images. In this section, we will describe the modifications used to extend it from a fixed gantry angle to CBCT projections.

The algorithm is a 2-step, iterative method that alternates between constraining the search window and running DP. A completely stationary FM with a 3D location $L_{3D} = (x, y, z)$ and a kV imager angle θ would project to:

$$\begin{aligned} P_u\left(L_{3D}, \theta, s\right) &= \frac{-x\cos\theta - z\sin\theta}{T} + UC \\ P_v\left(L_{3D}, \theta, s\right) &= \frac{y}{T} + VC + s \cdot RPM \\ T &= \left(-x\sin\theta + z\cos\theta + SAD\right) \cdot \frac{PS}{SID} \end{aligned} \tag{3.1}$$

where SAD is the source-to-axis distance; SID is the source-to-image distance; PS is the detector pixel size; UC and VC are the projected (u, v) coordinates of the isocenter;

RPM is the respiratory surrogate signal value; and s is the scaling factor for RPM.

Since the FM is not completely stationary, this set of (P_u, P_v) is used as the centers of 100×100 pixel search windows (approximately 23×23 mm) in each CBCT projection acquired from angle θ. For the first iteration, the 3D location L_{3D} comes from the contoured FM location from the planning CT, and $s = 0$.

The second step is the DP step, in which the cost function $f\left(p_1, p_2, \ldots, p_N\right)$ is minimized. Each p_i is a vector of all the possible FM locations in image i, and N is the total number of projection images. The radiopaque FMs have a lower intensity value than surrounding pixels and therefore, the list of possible locations corresponds to all of the local intensity minima in the search window.

The DP optimization algorithm is used to find the (u_i, v_i) in each p_i such that the following cost function is minimized:

$$f\left(p_1, p_2, \ldots, p_N\right) = \sum_{i=1}^{N} g\left(p_i\right) + \alpha \sum_{i=1}^{N} h\left(p_i\right) + \beta \sum_{i=1}^{N-1} k\left(p_i, p_{i+1}\right) \tag{3.2}$$

where

$$\begin{aligned} g\left(p_i\right) &= \sqrt{\left(u_i - c_{u,i}\right)^2 + \left(v_i - c_{v,i}\right)^2} \\ h\left(p_i\right) &= I\left(u_i, v_i\right) \\ k\left(p_i, p_{i+1}\right) &= \sqrt{\left(u_i - u_{i+1}\right)^2 + \left(v_i - v_{i+1}\right)^2}. \end{aligned} \tag{3.3}$$

$g\left(p_i\right)$ is the Euclidean distance from the center of the search window $\left(c_{u,i}, c_{v,i}\right) = \left(P_u\left(L_{3D}, \theta_i, s\right), P_v\left(L_{3D}, \theta_i, s\right)\right)$ to the minima (u_i, v_i); $k\left(p_i, p_{i+1}\right)$ is the Euclidean distance between possible minima in adjacent images i and $i + 1$; $h\left(p_i\right)$ is the linearly rescaled grayscale intensity value I such that the extreme values for the pixels in each p_i are 0 and 1; and $\alpha = 35$ and $\beta = 10$ are weighting parameters that were determined empirically.

After the DP step, the algorithm returns to step 1 with refined search windows (new L_{3D} and s) such that the sum of distances between the set of projected 3D FM locations (P_u, P_v) and the set of DP-tracked location (u_i, v_i) over all of the projections is minimized:

$$f\left(L_{3D}, s\right) = \sum_{i=1}^{N} \sqrt{\left[P_u\left(L_{3D}, \theta_i, s\right) - u_i\right]^2 + \left[P_v\left(L_{3D}, \theta_i, s\right) - v_i\right]^2}\,. \qquad \textbf{(3.4)}$$

The algorithm alternates between optimizing (u_i, v_i) by minimizing Equation 3.2 and optimizing L_{3D} and s by minimizing Equation 3.4 until less than 1% of the predicted locations change between iterations. In general, 2-3 iterations are required for convergence. The set of (u_i, v_i) for each CBCT projection i from the final iteration comprise the output FM locations from our tracking algorithm.

When tracking multiple FMs, the DP step is applied sequentially to each FM individually, and the search windows are constrained such that all the FMs are assumed to move together rigidly.

The DP tracking algorithm was evaluated on CBCT projection data sets acquired on 39 gated patients over a 2.5 year period at our institution (Institution A). To assess the accuracy of the algorithm, all FMs in all CBCT projections were segmented manually for each patient and used as the ground truth for comparison. The centroids of these manually segmented true FM locations were then compared to the DP-tracked locations.

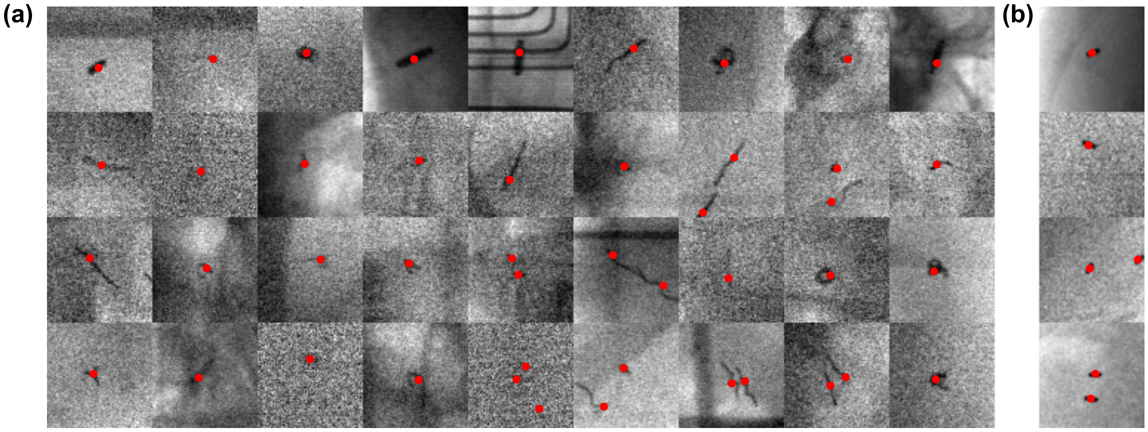

Figure 3.1: Examples of CBCT projections with the different FMs from **(a)** Institution A and **(b)** Institution B on which the DP algorithm was used. Each block is 16×16 mm. The red dots represent the DP tracked FM location. Note that for the very small FMs, the red dot may completely cover them.

The tracked FM locations can then be used clinically to automatically set up the patient. Use of the DP tracking algorithm for automatic patient setup was tested for two different setup strategies at two different institutions as described in the following. In both cases, the FM positions in the intrafraction fluoroscopic images were used to quantify the setup accuracy.

Figure 3.1 shows examples of the different FMs tracked using the DP algorithm from both institutions, and Table 3.1 summarizes the patient data characteristics.

3.2.2 Gating with Marker PTV

In Institution A, patients were gated based on the RPM external surrogate signal. The current manual setup (MS) standard is to first match the FMs from the reconstructed CBCT to those in the planning CT, and then to acquire anterior-posterior and lateral kV fluoroscopies to verify that the FMs were within the contoured gating

Table 3.1: Summary of patient data. *The numbers represent the number of patients in each category.

	CBCT Tracking (Institution A)	**Gating with mPTV (Institution A)**	**Mean Marker Position (Institution B)**
Number of patients	39	8	6
Fractions per patient in analysis (Range)	1	5.0 ± 4.8 (1-14)	2.7 ± 0.5 (2-3)
FM type*			
Visicoil	34	8	0
Gold seed	1	0	6
Calypso	2	0	0
Embolization coil	2	0	0
FMs per patient*			
1	10	2	0
2	16	3	1
3	7	1	5
4	6	2	0
Tumor site*			
Liver	17	3	6
Pancreas	12	4	0
Abdomen	5	0	0
Lung	5	1	0
CBCT parameters	110kV 20mA 20ms	125kV 20mA 15ms	125kV 80mA 15ms
Machine	Varian Trilogy	Varian TrueBeam	Varian TrueBeam
CBCT projections (Range)	642 ± 32 (460-673)	894	894
Intrafraction imaging frequency*			
Every 3 seconds		7	6
Every 15 seconds		1	0
Number of intrafraction images (Range)			
Every 3 seconds		88 ± 58 (35-320)	85 ± 20 (41-116)
Every 15 seconds		10 ± 1 (10-11)	

volume, mPTV, during beam on. The mPTV contour is typically created by extending the FM contour on the planning CT by 3-5 mm in all directions.

With the DP-tracked FM locations, the following equation can be minimized to find the optimal FM location L_{3D} and lower and upper gating bounds G_L and G_H:

$$\begin{aligned} f\left(L_{3D}, G_L, G_H\right) &= w_1\left\{(1-ACC)+v\left[\min\left(0, ACC-0.95\right)\right]^2\right\} \\ &\quad + w_2\left\{(1-DC)+v\left[\min\left(0, DC-0.5\right)\right]^2\right\} \end{aligned} \tag{3.5}$$

where the beam accuracy ACC and the duty cycle DC are

$$\begin{aligned} ACC &= \frac{\text{\# of images with beam on and marker inside mPTV}}{\text{\# of images with beam on}} \\ DC &= \frac{\text{\# of images with beam on}}{\text{total \# of images}}. \end{aligned} \tag{3.6}$$

$w_1 = 0.8$, $w_2 = 0.2$, and $v = 20$ are weighting parameters that were determined empirically. The beam is on when the RPM signal is between G_L and G_H (Figure 3.2). The 3D contoured mPTV from the planning CT is projected onto each image to determine the boundaries of the allowed FM motion. For multiple FMs, 2/3 of the FMs must be inside the mPTV when the beam is on to be considered accurate.

Equation 3.5 optimizes L_{3D}, G_L, and G_H by balancing beam accuracy ACC with duty cycle DC, with additional penalties enforced when accuracy drops below 95% and duty cycle below 50%. A further assumption of this equation is that the patient is gated on exhale. The optimal shift is the difference between the original and final L_{3D} locations, and the optimal gating bounds are G_L and G_H.

To evaluate the performance of our automated patient setup, 40 CBCT projection

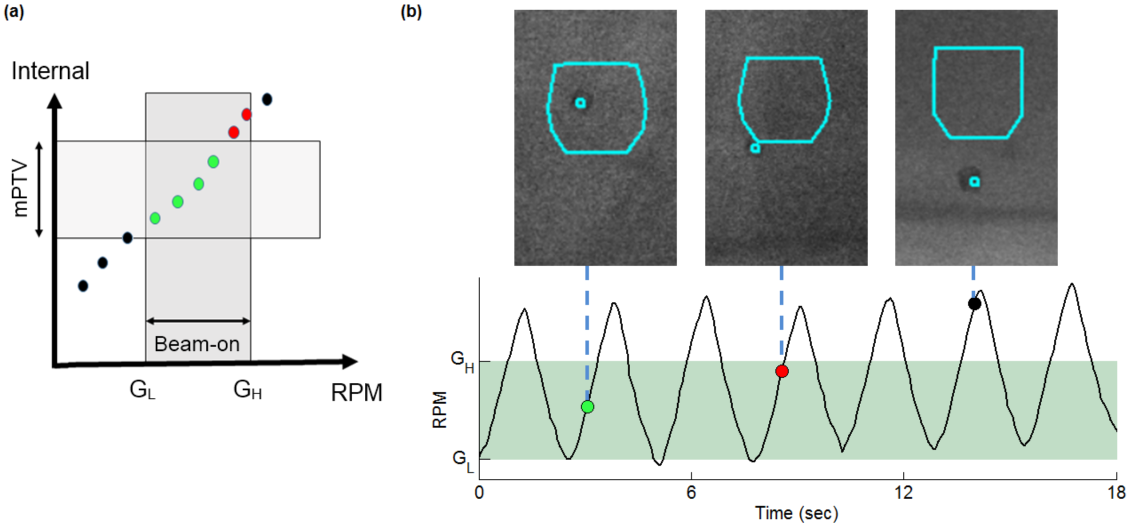

Figure 3.2: **(a)** Schematic of gating setup. In this example, accuracy $ACC = 4/6$ (green / green+red) and duty cycle $DC = 6/10$ (green+red / all). **(b)** Representative FM locations and mPTV projections corresponding to the color dots from (a). Note that the mPTV projections look different due to the different gantry angles in the 3 images.

data sets were collected for 8 gated patients over a 5 month period at Institution A. Intrafraction fluoroscopic images were acquired every 3 seconds during treatment with the exception of Patient A1 who had images acquired every 15 seconds, and the FMs were manually segmented in each image. These intrafraction images represent the true FM locations during treatment, and were therefore used as the ground truth. The mPTVs were projected onto the intrafraction images for both the DP-optimized and MS couch positions, and the manually segmented FM locations were then used to determine whether the FM was inside the mPTV. Finally, Equation 3.6 was used to calculate the accuracy and duty cycle.

3.2.3 Mean Marker Position

In Institution B, patients were set up to the mean marker position and not gated. The current MS standard is to match each FM individually in the reconstructed CBCT to the planning CT, and then calculating the mean position. This matching is done by estimating the center of mass from the often blurred FM in the reconstruction.

The targeted 3D FM location is such that the sum of distances between the projected 3D location and DP-tracked location over all of the projections is minimized. Therefore, we simply find the L_{3D} that minimizes Equation 3.4 with $s = 0$, and the optimal shift for patients setup to the mean marker position is the difference between the original and final L_{3D} locations.

To evaluate the performance of our automated patient setup, 16 CBCT projection data sets were collected for 6 patients over a 5 month period at Institution B. Intrafraction fluoroscopic images were acquired every 3 seconds during treatment, and the FMs were manually segmented in each image. Using Equation 3.4 with $s = 0$ and (u, v) being the manually segmented location, the optimal L_{3D} was computed using a least squares method. This optimal L_{3D} was then compared to the DP and MS L_{3D}s.

3.3 Results

Using the 87 manually segmented FMs for the 39 patients as the ground truth, the mean of the absolute 2D error of the DP algorithm was 1.3 ± 1.0 mm.

Figure 3.3 shows the setup accuracy and duty cycle for the gated patients from Institution A. Using the paired t-test, the DP algorithm is shown to improve the accuracy

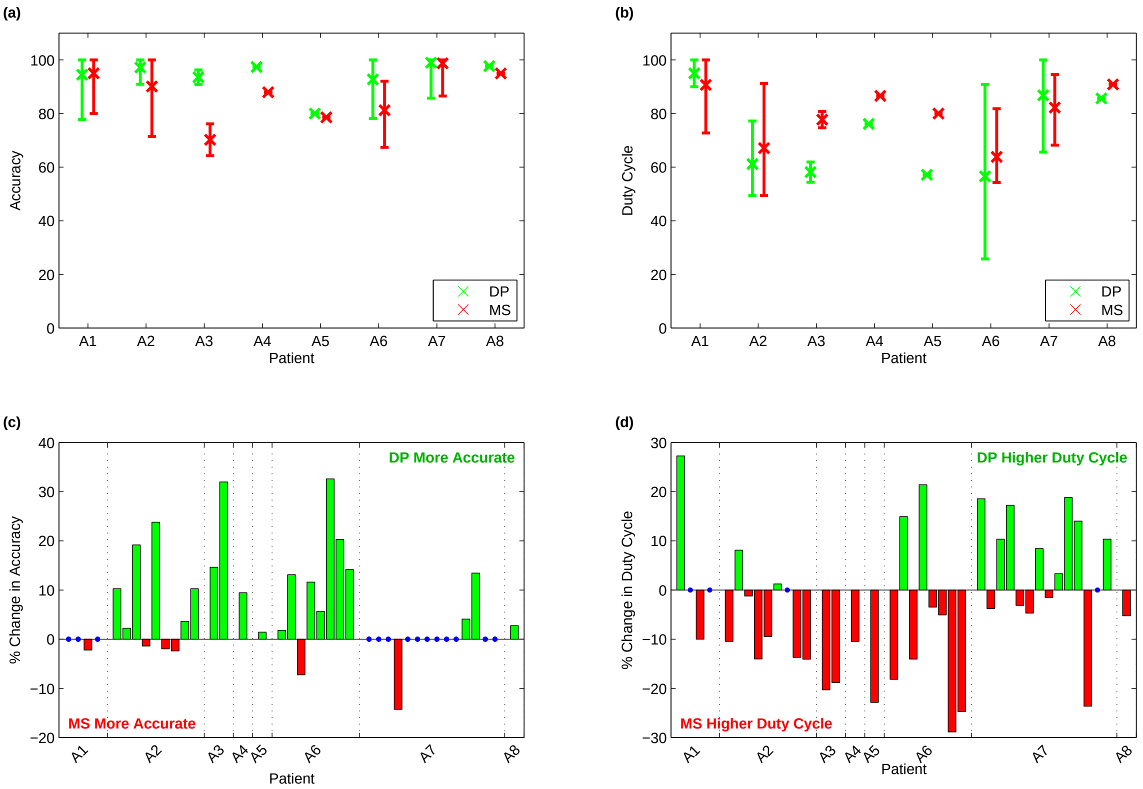

Figure 3.3: DP and MS **(a)** accuracy and **(b)** duty cycle by patient for Institution A. The X's indicate the mean with the bars indicating the minimum and maximum. Changes in DP and MS **(c)** accuracy and **(d)** duty cycle for Institution A. Each bar is a fraction, and the dotted black lines separate the fractions by patient. Blue dots represent fractions where there is no change in accuracy or duty cycle.

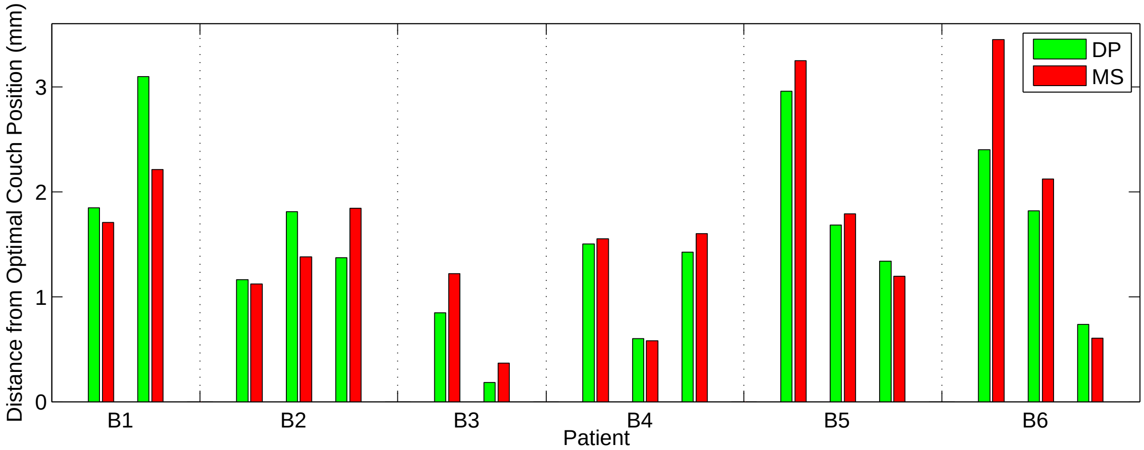

Figure 3.4: Setup error compared to optimal couch position for DP and MS for each fraction from Institution B.

of the setup when compared to the MS currently used clinically ($96 \pm 6\%$ vs $91 \pm 11\%$, $p < 0.01$) without a significant decrease in duty cycle ($73 \pm 19\%$ vs $76 \pm 13\%$, $p = 0.23$).

Figure 3.4 shows the setup errors for the non-gated patients from Institution B. It plots the difference between the DP and actual mean position as calculated from the intrafraction images, as well as the difference between the MS and actual mean position. The mean difference over all of the fractions for the DP position is 1.5 ± 0.8 mm while the mean difference for the MS position is 1.6 ± 0.9 mm. A paired t-test shows that the DP algorithm performs as well as the MS currently used clinically ($p = 0.48$).

3.4 Discussion

Patients with abdominal or thoracic tumors are typically set up by manually registering the pre-treatment CBCT to the planning CT. Often, this alignment is based on FMs implanted near the tumor site, which appear blurred in the reconstructed CBCT due to respiratory motion. This manual alignment process is very time intensive, user dependent, and requires a significant amount of user training. We have demonstrated a fully automatic algorithm that optimizes the patient couch position and/or gating bounds based on the tracked FMs in the CBCT projections. The algorithm takes 1-2 seconds to run, and is therefore much faster than the several to tens of minutes needed by the therapists/physicists to perform the task manually.

For the 87 FMs from the 39 patients, we showed that the mean of the absolute 2D error of the DP algorithm was 1.3 ± 1.0 mm to the centroid of each FM. There was no significant difference between the errors for the different anatomical sites. Therefore, all sites were grouped together in our analysis. In general, the larger FMs had larger errors. The DP algorithm assumes that the FM is at a local intensity minima, and multiple local minima may exist on a single large FM. Therefore, the tracked location from DP can jump around on the FM and not necessarily at the centroid, as can be seen in Figure 3.1.

Other methods in the literature that track FMs in CBCT projections are all based on template matching, and most require that the FMs be of a specific, known shape, typically spheres and cylinders. Some require the user to manually select the FMs in the first frame [28, 39] while another requires that the user manually define a region of interest that fully encompasses the FM's range of motion [38]. A few other studies do not require user inputs. They either use the planning CT to get an initial region of interest [36, 37] or they automatically create the templates using blob detection and rejecting those inconsistent with a 3D position [35]. A couple of recent studies can create templates for arbitrarily shaped FMs but require significant user intervention. Poulsen, et al. [40] requires the user to manually segment the FMs in 5 CBCT projections with no background obstructions. Regmi, et al. [41] automatically creates the templates from the planning CT, but requires manual adjustments of the templates when there are changes in the distances between FMs on the CBCT and planning CT, and requires the user to make manual adjustments when tracking fails in an image.

The biggest advantage to our DP approach over these other methods is that it is capable of accurately tracking FMs of arbitrary shape and size without any user intervention, and can therefore be more readily incorporated into the current clinical workflow. Furthermore, this is the first study, to our knowledge, that performs such marker tracking and patient setup optimization on data from multiple institutions. To validate and compare our DP-optimized patient setup to the current MS used for treatment, intrafraction images were acquired during treatment at two different institutions. This provided the real gold standard, as the true FM location during treatment was known. After manually segmenting the FM locations in these intrafraction images, we were able to compare the performance between our DP algorithm and the current manual clinical setup.

Figure 3.3 shows that on the fractions from Institution A, the DP algorithm improved the accuracy of the treatment for gated patients significantly (96% vs 91%, $p < 0.01$) without a significant decrease in duty cycle (73% vs 76%, $p = 0.23$). Much of this difference can be attributed to the extra time needed by the therapists to setup the gated patients. Changing the gating bounds requires additional fluoroscopy imaging, and as a result, the therapists make adjustments only when absolutely necessary. In many cases, this resulted in a lower accuracy as the beam is still on when the FM has just left the mPTV, but is close enough to not warrant adjustments and additional imaging. In our optimization, the DP algorithm prioritizes accuracy over duty cycle, and as a result, many fractions showed an increase in accuracy at the expense of a slightly decreased duty cycle. However, this slight decrease in duty cycle would not have any impact on the overall treatment time, as the majority of the treatment time is spent on getting the patient into the machine and setup in the proper position.

Since there is often some patient movement throughout a single treatment session, the FMs may have shifted slightly between the time the CBCT was acquired and the start of the treatment. Therefore, the accuracy of the DP algorithm is not always 100%. For fraction 4 of Patient A7, DP had the greatest decrease in accuracy compared to MS. The DP optimization placed the FM very close to the edge of the mPTV, but the FM shifted slightly during treatment. As a result, the FM was often 1-2 pixels outside of the mPTV, which counts as inaccurate in our analysis.

Figure 3.4 shows that on the fractions from Institution B, the DP algorithm set up the non-gated patients to the mean marker position similarly compared to the manual clinical setup (1.5 ± 0.8 mm vs 1.6 ± 0.9 mm, $p = 0.48$). The therapists are trained to align the patients based on the mean marker position, and both methods yielded results close to the optimal couch position based on manually segmented FM locations in the intrafraction images.

The main disadvantage of our DP algorithm compared to the template matching based algorithms is that it cannot be used to track FMs during intermittent imaging. Future work will involve the combining of our DP algorithm with a template based one. By using the DP-tracked FMs from the CBCT, it is conceivable that high-quality 3D templates can be automatically generated. These templates can then be used to improve on the DP tracking similar to the DPTM algorithm from Chapter 2. Furthermore, the templates can also be used to track the FMs in real-time during intermittent intrafraction imaging to monitor the patient position throughout the course of a treatment.

In conclusion, we have shown that our DP-optimized patient setup is as good as or better than the current clinical setup at two different institutions. The biggest advantage of our algorithm is that it requires no user intervention and can provide the optimal setup before the CBCT has even been reconstructed. By automating the alignment process, we can greatly reduce the patient setup time, and for some institutions, also eliminate the extra pre-treatment imaging required.

Chapter 4

Tumor Tracking in Cine MR Images[†]

In the previous chapters, we tracked FMs, which act as surrogates to the tumors that cannot be seen with x-ray imaging. A combined MR/radiation delivery system allows for direct visualization of the moving tumors. In this chapter, we propose a new method that can automatically track the tumor in 2D cine-MR images. We further compare our algorithm tracking to manually segmented ground truths.

[†] The work in this chapter has been previously submitted for publication in [45].

4.1 Background and Significance

In January of 2014, the first cancer patient was treated using the ViewRay MRIdian [3]. Combining MR imaging with a radiation delivery system, the MRIdian allowed physicians to see real-time tumor motion during treatment for the first time. In February 2015, respiratory gating began. The system would automatically track a physician-drawn target and pause the radiation beam each time a certain percentage left a physician-assigned boundary. Despite the utility of this system, there remains a great deal of room for improvement on the accuracy and consistency with which it is able to track its target.

Thousands of papers have been published on the topic of tracking a specified moving target in videos. They range from simple pixelwise difference detection algorithms [46, 47] to more advanced methods that use mean shift [48], level sets [49], optical flow [50], and more. While these algorithms have been successfully used to track various targets, they have not been directly applied to the noisy, low resolution images obtained from the ViewRay system, which uses a 0.35T open bore magnet to obtain 2D images with a spatial resolution of 3.5 mm × 3.5 mm at 4 frames/second. To date, the only paper to track targets on the ViewRay system is by Mazur, et al. [51], which uses SIFT for feature matching. However, this algorithm requires significant user interaction to select the proper subregion layout and size, something that is too time consuming and labor intensive to be practical in a clinical setting. Furthermore, the complexity of the algorithm makes it too computationally slow (~250ms per image) to be used in real-time.

In order to minimize the amount of user interactions, we take advantage of a few key properties of the motion of the target in our images. First, the patient is stationary during the treatment. Second, the target, which may be the tumor or an organ, moves in a well-constrained path due to respiration. Therefore, all images acquired at the same point in the respiratory cycle should be almost identical. Due to this one-to-one correlation between the respiratory cycle and the image appearance, the tracking problem (which requires solving for motion and deformation of a part of the image) can be converted to a simpler problem of estimating the current phase of respiration. In this chapter, we demonstrate that principal component analysis (PCA) gives a model of image appearance sufficient to estimate this respiratory phase and therefore offers very fast approaches to tracking.

4.2 Materials and Methods

Figure 4.1 outlines the tracking algorithm, which consists of three components. First, we create a patient-specific model that maps the image appearance to the target contour by running PCA on the image data (Subsection 4.2.1). The images are binned into clusters based on their coefficients and an optimal contour of the target is derived for each bin. Next, during the patient treatment, we compute the PCA coefficients of each frame and look up the target contour from the closest bin (Subsection 4.2.2). Finally, we confirm that the PCA coefficients are close to those from the bin and retrain the model if they are not. We now discuss these parts separately in more detail (Subsection 4.2.2).

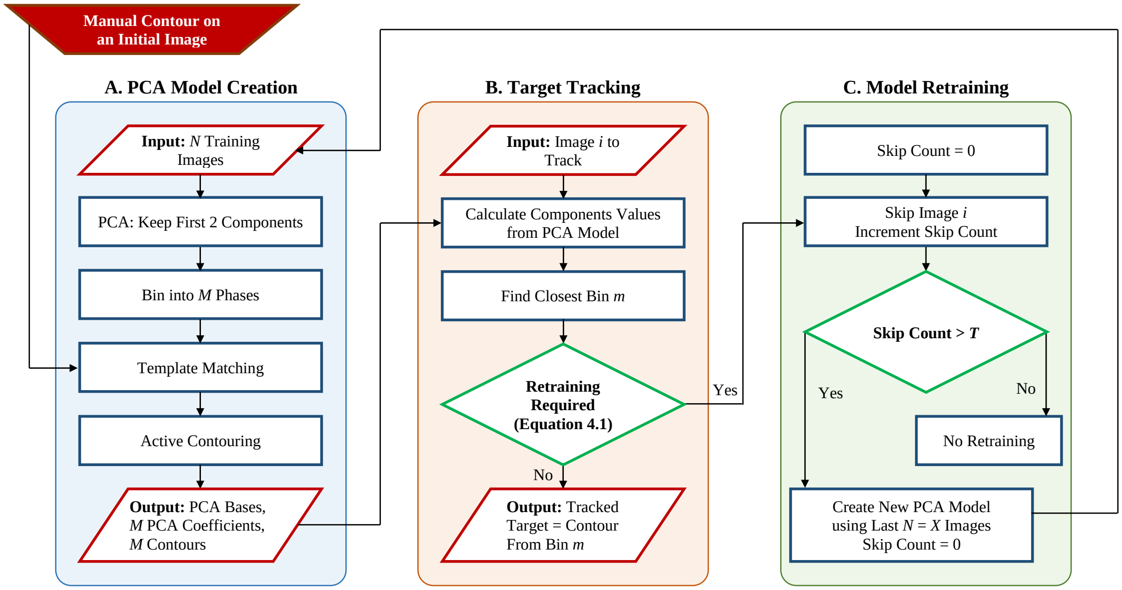

Figure 4.1: Flowchart of tracking algorithm.

4.2.1 PCA Model Creation

$N = 100$ training images are used to create the model. For our datasets, this equates to 25 seconds of imaging (approximately 5-8 breaths). Each of the N images is represented as a $p \times 1$ vector where p is the number of pixels per image. PCA is applied to the N vectors and the first two components ($PC1$ and $PC2$) are kept. This typically covers more than 98% of the variance and is therefore a good approximation of the data. Previous works have also shown that the first two components are sufficient to model respiratory motion using PCA [52, 53].

The N images are then binned into $M = 10$ equal-sized clusters, minimizing the Euclidean distance between $PC1$ and $PC2$, and the cluster centers. This does well to separate the images into M respiratory phases. Figure 4.2a plots the N images as represented by $PC1$ and $PC2$, with the median value of each bin indicated by the black Xs.

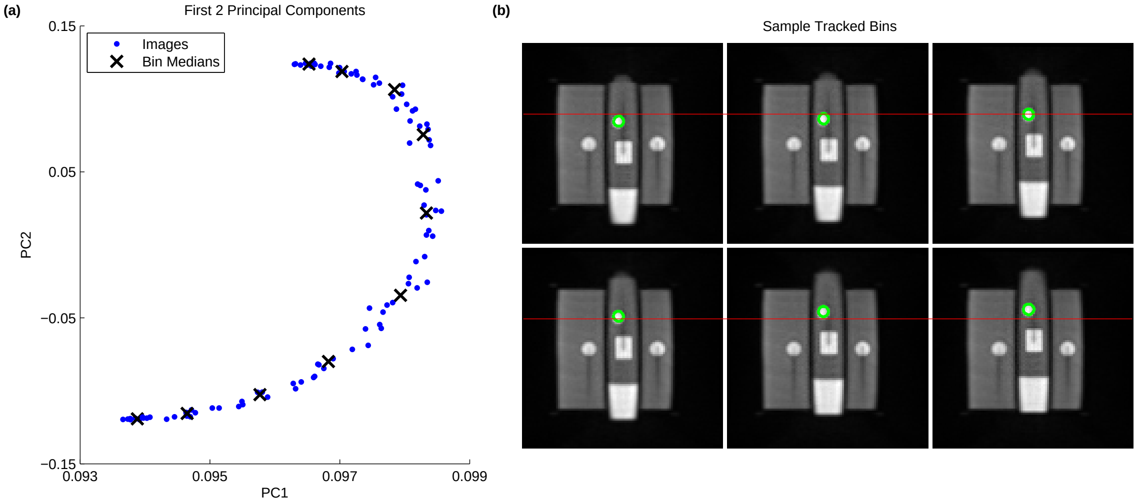

Figure 4.2: **(a)** Plot of $PC1$ and $PC2$ for $N = 100$ training images. The black Xs represent the median of each of the $M = 10$ bins. **(b)** Averaged images from bins 1, 3, 5, 6, 8, and 10, from top to bottom. The green circles represent the contoured target, and the red line is in the same position for all images for visual reference. The images shown are from a physical phantom where the middle section moves vertically with the two sides being stationary.

All images in each bin are pixelwise averaged together, greatly increasing the signal-to-noise ratio of the images and decreasing the noise. The target is tracked on these averaged images using template matching followed by active contouring. Figure 4.2b shows the averaged images from bins 1, 3, 5, 6, 8, and 10. The green circles represent the contoured target, and the red lines are at the same position for each image for easier visual comparison of the contoured target locations.

The template matching uses normalized cross correlation to find the best match to an initial, manually drawn contour of the target. The template used is a rectangular crop of the drawing on the contoured image. The matched contour is then used as the initialization for a region-based active contouring algorithm [54], which allows for deformations of the target in the different bins. For the active contouring algorithm, the means separation energy [55] function was used with parameters $\lambda = 0.2$ (smoothness constraint) and $r = \sqrt{N/8}$ (localization radius), where N is the number of pixels in the contour. If $r < 7$, then the image is upsampled such that $r = 7$. This ensures consistent parameters that work for targets of any size.

The PCA motion model consists of the PCA bases from the N training images, truncated to the first 2 components, the M median $PC1$ and $PC2$ values from each bin, and the M tracked contours from each bin. These outputs are then used to track the target on the new images.

4.2.2 Target Tracking

For each new image i to track, the PCA bases from the model are used to calculate $PC1$ and $PC2$. The nearest bin m is the one with the smallest Euclidean distance between the image and bin coefficients. Two distance metrics d_1 and d_2 are used to determine whether retraining is necessary:

$$\begin{aligned} d_1 &= |PC1_i - PC1_m| \\ d_2 &= |PC2_i - PC2_m| \end{aligned} \tag{4.1}$$

If both distances are within a set threshold ($d_1 < r_1$, $d_2 < 0.2 \cdot r_2$, where r_1 and r_2 are the differences between the minimum and maximum $PC1$ and $PC2$ values, respectively, for all M bins), then the tracked contour for image i is the contour from bin m. Otherwise, tracking is skipped on image i, and the skip counter is incremented by 1. If this skip counter exceeds a threshold $T = 20$, then the model is retrained.

4.2.3 Model Retraining

To retrain the model, the same algorithm as described in Subsection 4.2.1 is used, but with the previous $N = 480$ images (2 minutes worth) instead of the initial 100 training images. The target contour is not redrawn; the same initial manually drawn contour is used for the template matching. This newly created model is then used for subsequent tracking. Finally, the skip counter is reset to zero. The purpose of the retraining is to sporadically update the model to account for any changes in the target motion patterns over time.

4.2.4 Test Data

Data was collected from a physical phantom (Figure 4.2) and 17 patients imaged on the ViewRay MRIdian machine. This 0.35T MR acquired images using a balanced steady-state free precession sequence (Siemens TrueFISP). Typical scan parameters are $TR = 2.1$ms, $TE = 0.91$ms, and a low flip angle.

2D sagittal cine MR images were acquired at 4 frames/second, with a 7mm slice thickness and a 3.5 mm $\times$ 3.5 mm (100×100 pixels) in-plane spatial resolution. The mean number of images per patient was 4600 ± 2200 (19 ± 9 minutes). For each data set, an initial contour was manually drawn on the first image, and the first 100 images were used for the model training.

The algorithm was run on each data set twice using the same initial manually drawn contour: once with the model retraining and once without. When retraining was not performed, the output contour was from the closest bin, regardless of whether d_1 and d_2 were within the set threshold.

To validate the tracking accuracy of our algorithm, the output contours were compared to manually contoured targets on 2 sets of 100 images per patient. The 1st set of 100 were from the images immediately following the training set, and the 2nd set were the last images from each data set. The Dice similarity coefficient (DSC) and the modified Hausdorff distance (MHD) [56] were used to quantify the comparisons. The metrics are defined as:

$$\begin{aligned} \text{DSC} &= \frac{2\left|S_m \cap S_t\right|}{\left|S_m\right| + \left|S_t\right|} \\ \text{MHD} &= \frac{1}{\left|B_m\right|} \sum_{m \in B_m} \min_{t \in B_t} \|m - t\| \end{aligned} \tag{4.2}$$

where S_m and S_t denote the manual and tracking algorithm segmentations, respectively, and B_m and B_t denote the boundary points on S_m and S_t, respectively.

4.3 Results

Figure 4.3 shows a sample tracking result of our algorithm from each of the data sets. Figures 4.4a and 4.4b show the DSC and MHD, respectively, for each data set for the first set of 100 images and the second set of 100 images with and without model retraining. Figures 4.4c and 4.4d show the mean DSC and MHD, respectively, for the phantom and over all of the patients.

The mean DSC for the phantom was 0.90 ± 0.04 for the 1st set and 0.89 ± 0.04 for the 2nd, while the mean MHD were 0.40 ± 0.16 pixels (1st set) and 0.44 ± 0.17 pixels (2nd set).

No retraining occurred on the phantom data set. For the 17 patients, the mean num-

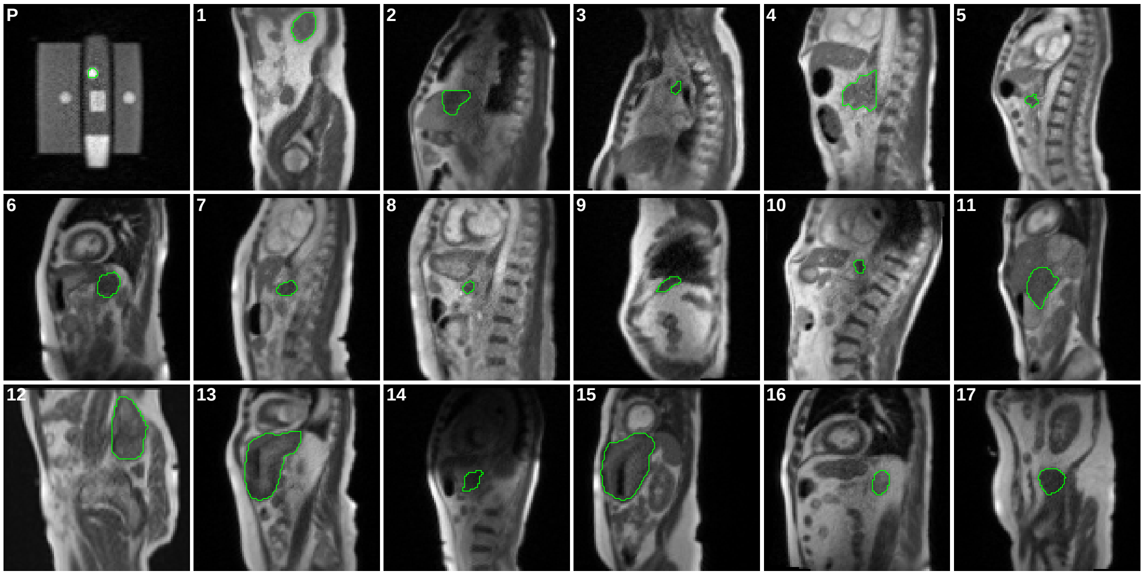

Figure 4.3: Examples of the tracked target from the physical phantom (P) and the 17 patients.

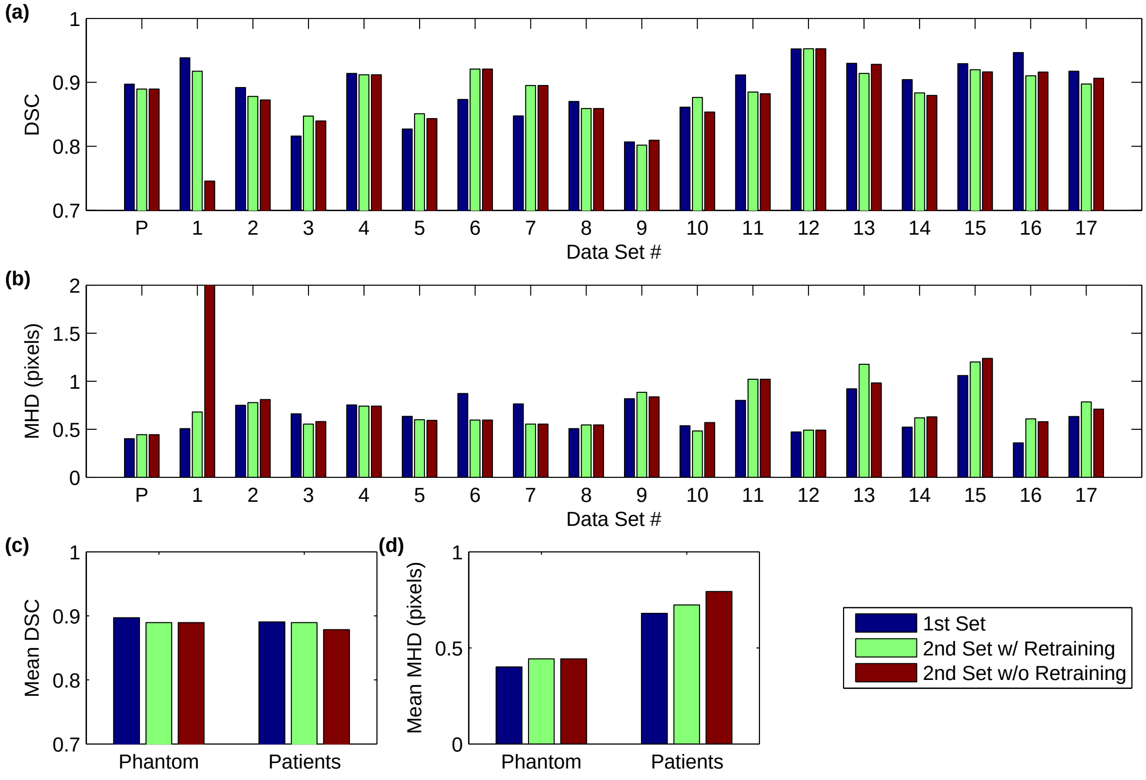

Figure 4.4: **(a)** DSC and **(b)** MHD for each data set. Data set P is from the physical phantom. Mean **(c)** DSC and **(d)** MHD for phantom and patients.

ber of retrains was 1.4 ± 1.4. Five of the patients did not require retraining, while Patients 1 and 13 required the most number of retrains (4 and 5, respectively).

The mean DSC over all of the patients for the 1st set was 0.89 ± 0.05, while the mean DSC for the 2nd set were 0.89 ± 0.04 with retraining and 0.88 ± 0.05 without retraining. A paired t-test showed no statistical difference between the 1st set and 2nd set with retraining ($p = 0.82$) and no significant difference between the 2nd set with and without retraining ($p = 0.29$).

The mean MHD over all of the patients for the 1st set was 0.68 ± 0.18 pixels, while the mean MHD for the 2nd set were 0.72 ± 0.23 with retraining and 0.79 ± 0.38 without retraining. Similarly, a paired t-test showed no statistical difference between the 1st set and 2nd set with retraining ($p = 0.22$) and no significant difference between the 2nd set with and without retraining ($p = 0.40$).

4.4 Discussion

Figure 4.3 shows examples of the targets that were tracked by our algorithm. The targets vary in size, shape, and contrast. However, with guidance from just a single manually drawn contour, our algorithm was able to successfully track the motion and deformations of the target over the entire imaging session.

From the training data, the images were separated into 10 bins based on the first two PCA coefficients and averaged pixelwise. Segmentation of the target was then performed on the averaged images. This averaging greatly increases the contrast and decreases the noise in the images, making the segmentation process more robust compared to segmentation on individual images. For each new image to be tracked, the

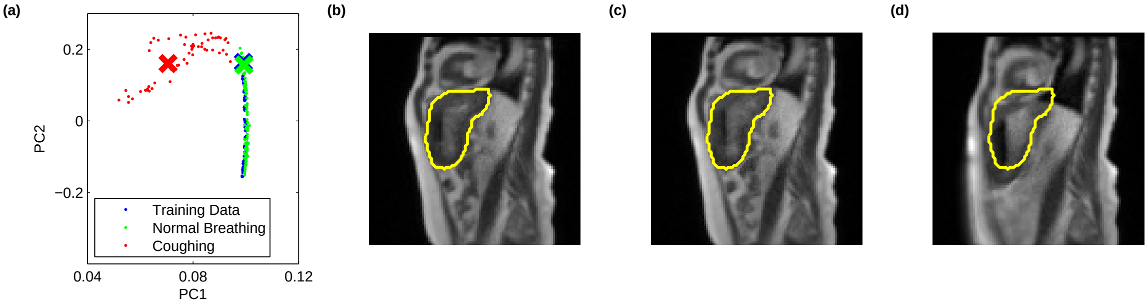

Figure 4.5: **(a)** Plot of $PC1$ and $PC2$ for 100 images from training data, 100 images from normal breathing, and 60 images from a coughing fit. An image from **(b)** training, **(c)** normal breathing, and **(d)** coughing corresponding to the Xs from (a). The yellow is the contour from the closest bin. Note the good match during normal breathing and poor match during coughing.

PCA model is used to determine the bin that contains images closest in appearance to the new one. If the closeness criteria of Equation 4.1 is met, then the contour of the bin is assigned as the contour for the new image. We chose to use $M = 10$ bins as a compromise between the number of images available to average per bin to decrease noise and the number of bins needed to accurately capture the motion.

Figure 4.5 shows an example of how the PCA coefficients relate to the image appearance. With normal breathing, the coefficients are similar to those from the training data. However, if a drastic change occurs, such as the patient coughing, then the coefficients are far away and exceed the Equation 4.1 thresholds, resulting in unreliable tracking. In a clinical setting, the radiation beam would be turned off when the algorithm determines such unreliable tracking.

In our physical phantom study, we imaged a 1-inch sphere being moved up and down in a sinusoidal pattern at 0.5 Hz with a peak-to-peak amplitude of 3 cm (Figure 4.2b). This speed and magnitude of motion represents a worst case scenario when compared to normal breathing patterns, which typically result in motions up to 1-2 cm at 0.2-0.3 Hz. Figure 4.6 shows zoomed-in versions of an image of the phantom to be tracked,

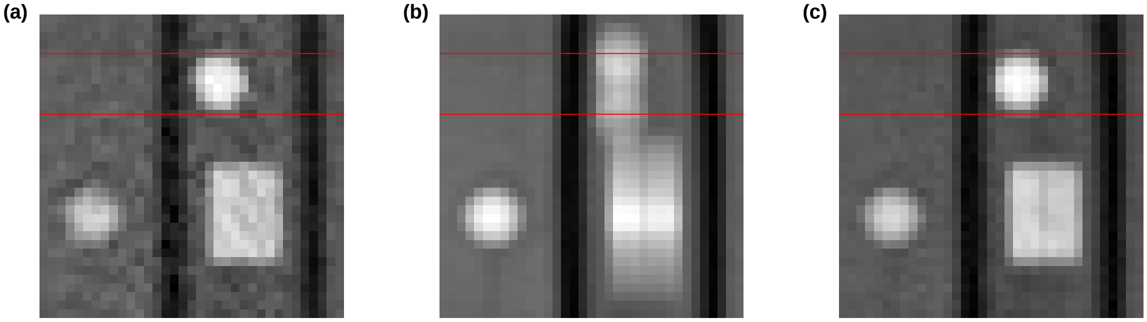

Figure 4.6: **(a)** Zoomed-in version of the image to be tracked, closest to bin 6 from Figure 4.2a. **(b)** PCA reconstruction of image using first two components. **(c)** Bin 6 averaged image on which tracking is performed. The red lines are in the same location for reference.

the PCA reconstructed image using the first two components, and the averaged image from the nearest bin. Due to the large motion, the reconstruction is not very good, with clearly visible blurring of the sphere. However, this does not affect the tracking accuracy since tracking is performed on the averaged image of the bin, which exhibits no motion blurring.

For the phantom data, the target location was manually contoured in 200 images in the same way as for the patient targets. Due to the poor resolution of the system (3.5 mm/pixel) and the relatively small size of the target (~7 pixels in diameter), the manual contours provide a better ground truth for comparison as they take into account the target manual contouring uncertainties also present in the patient targets. Tracking on the phantom resulted in a mean DSC of 0.90 and mean MHD of 0.42 pixels, both of which indicate good tracking accuracy. We chose to analyze both metrics as the DSC can be skewed higher for larger targets. For radiation therapy purposes, the accuracy at the target boundaries is very important, and therefore the MHD provides a useful metric of comparison.

For both the phantom and the patients, the analyses were performed on two sets of 100 images, the 1st being the 100 images immediately after the initial training,

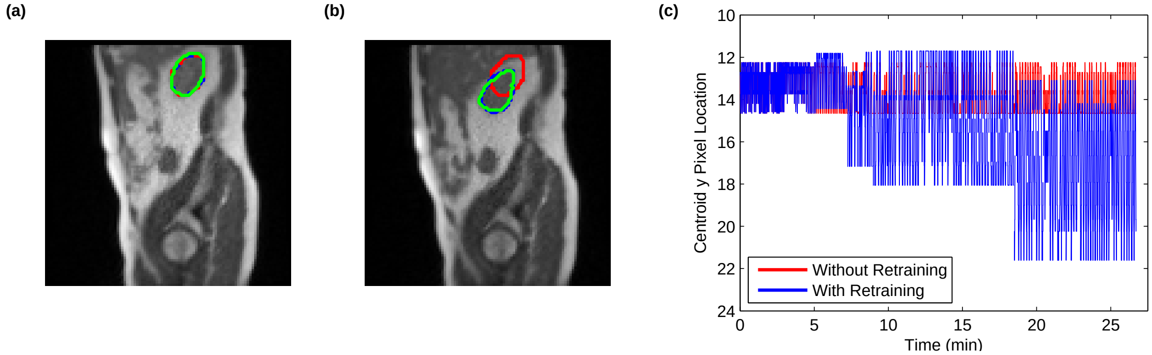

Figure 4.7: Sample tracking result for patient 1 from the **(a)** 1st and **(b)** 2nd sets. Red is without retraining, blue is with retraining, and green is the manually contoured ground truth. **(c)** Target centroid y position over the course of the 27 minute treatment.

and the 2nd being the last 100 images of the data set. The two sets were then compared to each other to see if the tracking remained consistent throughout the entire treatment despite the automatic model retrainings and changes in the images due to organ motions or other physiological effects (Figure 4.4). The overall mean DSC for the patients was 0.89 ± 0.04 and the mean MHD was 0.70 ± 0.20 pixels. A paired t-test showed no significant differences between the two sets. These results are similar to those obtained by Mazur et al. [51], who reported a mean DSC of 0.92 and a mean MHD of 0.40 pixels. The differences are likely due to contouring difficulties, which include targets that share boundaries with similar intensity structures, and noise that make it difficult to distinguish between target and background.

For the 17 patients, the mean number of retrains was 1.4. The purpose of the model retraining is to account for changes in the image appearances over time. Figure 4.7 shows that over the course of a 27 minute treatment, Patient 1's breathing patterns changed drastically after becoming more relaxed, going from fast, shallow breaths to slower, much deeper ones. As a result, the target motion in the y axis increased from about 2 pixels peak-to-peak to 8 pixels, causing errors up to 7 pixels (2.5 cm) at peak inhalation. The model retraining allowed our algorithm to successfully track the target despite these large respiratory changes.

For the other 16 patients, retraining appeared unnecessary, as the DSC and MHD were the same regardless of whether the retaining was performed. In most cases, the model retraining was triggered by atypically deep breaths not seen during training or normal movements in the gastrointestinal tract such as a passing of gas. For Patient 13, retraining was triggered by multiple coughing fits in the middle of the treatment. In these situations, the target appeared to resume its original motion trajectory afterwards, so little difference was seen in the tracking results with and without retraining. Retraining may be more relevant when tracking on images with higher spatial resolutions that can resolve smaller shifts in the motion trajectory. Since the appearance of the targets do not change significantly, the original contours can be reused during retraining.

Due to the simplifications that we made, we are able to correlate the PCA coefficients of a new image to the tracked contours. The calculation of the coefficients is extremely fast, requiring less than 1 ms per image. Our PCA approach to tumor tracking will be able to easily keep up with future technological advances of imaging systems with higher spatial and temporal resolutions.

In conclusion, we have developed an approach to real-time target tracking from MR data captured during radiation treatment. The approach detects failure of the model that arises during anomalies such as coughing or erratic motions. During such occurrences, both the tracking and the radiation beam are paused until the patient resumes normal breathing, preventing delivery of unexpected radiation doses. Furthermore, through model retraining, our algorithm is able to update the model and continue accurately tracking a target that drifts away from the initial, training trajectory. The minimal user intervention required by our algorithm (only an initial contour for tracking needs to be defined) allows it to be readily implemented in the clinic to aid in motion management, providing for a better radiation delivery with less toxicity to surrounding, healthy tissue.

References

[1] A. M. A. S. . D. Resources. *Physician characteristics and Distribution in the US*. Survey & Data Resources, American Medical Association, 2010.

[2] I. M. R. T. C. W. Group et al. Intensity-modulated radiotherapy: current status and issues of interest. *International Journal of Radiation Oncology, Biology, Physics*, 51(4):880–914, 2001.

[3] S. Mutic and J. F. Dempsey. The viewray system: Magnetic resonance–guided and controlled radiotherapy. In *Seminars in Radiation Oncology*, volume 24, pages 196–199, 2014.

[4] X. Y. Cedric, D. A. Jaffray, and J. W. Wong. The effects of intra-fraction organ motion on the delivery of dynamic intensity modulation. *Physics in Medicine and Biology*, 43(1):91, 1998.

[5] M. W. Kissick, S. A. Boswell, R. Jeraj, and T. R. Mackie. Confirmation, refinement, and extension of a study in intrafraction motion interplay with sliding jaw motion. *Medical Physics*, 32(7):2346–2350, 2005.

[6] F. J. Lagerwaard, J. R. V. S. de Koste, M. R. Nijssen-Visser, R. H. Schuchhard-Schipper, S. S. Oei, A. Munne, and S. Senan. Multiple slow ct scans for incorporating lung tumor mobility in radiotheraphy planning. *International Journal of Radiation Oncology, Biology, Physics*, 51(4):932–937, 2001.

[7] R. W. Underberg, F. J. Lagerwaard, B. J. Slotman, J. P. Cuijpers, and S. Senan. Use of maximum intensity projections (mip) for target volume generation in 4dct scans for lung cancer. *International Journal of Radiation Oncology, Biology, Physics*, 63(1):253–260, 2005.

[8] J. W. Wolthaus, C. Schneider, J.-J. Sonke, M. van Herk, J. S. Belderbos, M. M. Rossi, J. V. Lebesque, and E. M. Damen. Mid-ventilation ct scan construction from four-dimensional respiration-correlated ct scans for radiotherapy planning of lung cancer patients. *International Journal of Radiation Oncology, Biology, Physics*, 65(5):1560–1571, 2006.

[9] C. Beltran, M. G. Herman, and B. J. Davis. Planning target margin calculations for prostate radiotherapy based on intrafraction and interfraction motion using four localization methods. *International Journal of Radiation Oncology, Biology, Physics*, 70(1):289–295, 2008.

[10] C. Nelson, P. Balter, R. C. Morice, B. Choi, R. J. Kudchadker, K. Bucci, J. Y. Chang, L. Dong, S. Tucker, S. Vedam, et al. A technique for reducing patient setup uncertainties by aligning and verifying daily positioning of a moving tumor using implanted fiducials. *Journal of Applied Clinical Medical Physics*, 9(4), 2008.

[11] A. J. Nederveen, H. Dehnad, U. A. van der Heide, R. J. A. van Moorselaar, P. Hofman, and J. J. Lagendijk. Comparison of megavoltage position verification for prostate irradiation based on bony anatomy and implanted fiducials. *Radiotherapy and Oncology*, 68(1):81–88, 2003.

[12] J. M. Schallenkamp, M. G. Herman, J. J. Kruse, and T. M. Pisansky. Prostate position relative to pelvic bony anatomy based on intraprostatic gold markers and

electronic portal imaging. *International Journal of Radiation Oncology, Biology, Physics*, 63(3):800–811, 2005.

[13] A. M. Nichol, K. K. Brock, G. A. Lockwood, D. J. Moseley, T. Rosewall, P. R. Warde, C. N. Catton, and D. A. Jaffray. A magnetic resonance imaging study of prostate deformation relative to implanted gold fiducial markers. *International Journal of Radiation Oncology, Biology, Physics*, 67(1):48–56, 2007.

[14] A. Raaijmakers, B. Raaymakers, and J. Lagendijk. Integrating a mri scanner with a 6 mv radiotherapy accelerator: dose increase at tissue–air interfaces in a lateral magnetic field due to returning electrons. *Physics in Medicine and Biology*, 50(7):1363, 2005.

[15] D. Saenz, J. Bayouth, and B. Paliwal. Su-e-t-614: A comparison of imrt plans for the viewray mr-guided rt system with tomotherapy and pinnacle. *Medical Physics*, 40(6):347–347, 2013.

[16] D. L. Saenz, B. R. Paliwal, J. E. Bayouth, et al. A dose homogeneity and conformity evaluation between viewray and pinnacle-based linear accelerator imrt treatment plans. *Journal of Medical Physics*, 39(2):64, 2014.

[17] J. Dempsey, B. Dionne, J. Fitzsimmons, A. Haghigat, J. Li, D. Low, S. Mutic, J. Palta, H. Romeijn, and G. Sjoden. We-e-vala-06: A real-time mri guided external beam radiotherapy delivery system. *Medical Physics*, 33(6):2254–2254, 2006.

[18] H. Wan, J. Ge, and P. Parikh. Using dynamic programming to improve fiducial marker localization. *Physics in Medicine and Biology*, 59(8):1935, 2014.

[19] S. B. Jiang. Radiotherapy of mobile tumors. In *Seminars in Radiation Oncology*, volume 16, pages 239–248. Elsevier, 2006.

[20] G. D. Hugo, N. Agazaryan, and T. D. Solberg. An evaluation of gating window size, delivery method, and composite field dosimetry of respiratory-gated imrt. *Medical Physics*, 29:2517, 2002.

[21] N. M. Wink, M. Chao, J. Antony, and L. Xing. Individualized gating windows based on four-dimensional ct information for respiration-gated radiotherapy. *Physics in Medicine and Biology*, 53(1):165, 2008.

[22] R. Wiersma and L. Xing. Examination of geometric and dosimetric accuracies of gated step-and-shoot intensity modulated radiation therapy. *Medical Physics*, 34:3962, 2007.

[23] X. A. Li, C. Stepaniak, and E. Gore. Technical and dosimetric aspects of respiratory gating using a pressure-sensor motion monitoring system. *Medical Physics*, 33:145, 2006.

[24] A. Nederveen, J. Lagendijk, and P. Hofman. Detection of fiducial gold markers for automatic on-line megavoltage position verification using a marker extraction kernel (MEK). *International Journal of Radiation Oncology, Biology, Physics*, 47(5):1435–1442, July 2000.

[25] A. Nederveen, J. Lagendijk, and P. Hofman. Feasibility of automatic marker detection with an a-si flat-panel imager. *Physics in Medicine and Biology*, 46(4):1219, 2001.

[26] A. J. Nederveen, U. A. Heide, H. Dehnad, R. J. A. Moorselaar, P. Hofman, and J. J. Lagendijk. Measurements and clinical consequences of prostate motion during a radiotherapy fraction. *International Journal of Radiation Oncology, Biology, Physics*, 53(1):206–214, 2002.

[27] H. Shirato, S. Shimizu, T. Kunieda, K. Kitamura, M. van Herk, K. Kagei, T. Nishioka, S. Hashimoto, K. Fujita, H. Aoyama, K. Tsuchiya, K. Kudo, and K. Miyasaka. Physical aspects of a real-time tumor-tracking system for gated radiotherapy. *International Journal of Radiation Oncology, Biology, Physics*, 48(4):1187–1195, November 2000.

[28] X. Tang, G. C. Sharp, and S. B. Jiang. Fluoroscopic tracking of multiple implanted fiducial markers using multiple object tracking. *Physics in Medicine and Biology*, 52(14):4081–98, July 2007.

[29] J. M. Balter, K. L. Lam, H. M. Sandler, J. F. Littles, R. L. Bree, and R. K. Ten Haken. Automated localization of the prostate at the time of treatment using implanted radiopaque markers: technical feasibility. *International Journal of Radiation Oncology, Biology, Physics*, 33(5):1281–6, December 1995.

[30] L. A. Dawson, D. W. Litzenberg, K. K. Brock, M. Sanda, M. Sullivan, H. M. Sandler, and J. M. Balter. A comparison of ventilatory prostate movement in four treatment positions. *International Journal of Radiation Oncology, Biology, Physics*, 48(2):319–323, 2000.

[31] P. A. Kupelian, A. Forbes, T. R. Willoughby, K. Wallace, R. R. Mañon, S. L. Meeks, L. Herrera, A. Johnston, and J. J. Herran. Implantation and stability of metallic fiducials within pulmonary lesions. *International Journal of Radiation Oncology, Biology, Physics*, 69(3):777–785, 2007.

[32] J. C. Hong, Y. Yu, A. K. Rao, S. Dieterich, P. G. Maxim, Q.-T. Le, M. Diehn, D. Y. Sze, N. Kothary, and B. W. Loo. High retention and safety of percutaneously implanted endovascular embolization coils as fiducial markers for image-guided

stereotactic ablative radiotherapy of pulmonary tumors. *International Journal of Radiation Oncology, Biology, Physics*, 81(1):85–90, 2011.

[33] R. Bellman. On the theory of dynamic programming. *Proceedings of the National academy of Sciences of the United States of America*, 38(8):716, 1952.

[34] H. Wan, J. Bertholet, J. Ge, P. Poulsen, and P. Parikh. Automated patient setup and gating using cone beam computed tomography projections. *Physics in Medicine and Biology*, 61(6):2552, 2016.

[35] W. Fledelius, E. Worm, U. V. Elstrø m, J. r. B. Petersen, C. Grau, M. Hø yer, and P. R. Poulsen. Robust automatic segmentation of multiple implanted cylindrical gold fiducial markers in cone-beam CT projections. *Medical Physics*, 38(12):6351–61, December 2011.

[36] W. Mao, R. D. Wiersma, and L. Xing. Fast internal marker tracking algorithm for onboard MV and kV imaging systems. *Medical Physics*, 35(5):1942–9, May 2008.

[37] J. C. Park, S. H. Park, J. H. Kim, S. M. Yoon, S. S. Kim, J. S. Kim, Z. Liu, T. Watkins, and W. Y. Song. Four-dimensional cone-beam computed tomography and digital tomosynthesis reconstructions using respiratory signals extracted from transcutaneously inserted metal markers for liver sbrta). *Medical Physics*, 38(2):1028–1036, 2011.

[38] R. D. Wiersma, W. Mao, and L. Xing. Combined kV and MV imaging for real-time tracking of implanted fiducial markers. *Medical Physics*, 35(4):1191–8, April 2008.

[39] T. E. Marchant, A. Skalski, and B. J. Matuszewski. Automatic tracking of implanted fiducial markers in cone beam CT projection images. *Medical Physics*, 39(3):1322–34, March 2012.

[40] P. R. Poulsen, W. Fledelius, P. J. Keall, E. Weiss, J. Lu, E. Brackbill, and G. D. Hugo. A method for robust segmentation of arbitrarily shaped radiopaque structures in cone-beam CT projections. *Medical Physics*, 38(4):2151, March 2011.

[41] R. Regmi, D. M. Lovelock, M. Hunt, P. Zhang, H. Pham, J. Xiong, E. D. Yorke, K. A. Goodman, A. Rimner, H. Mostafavi, et al. Automatic tracking of arbitrarily shaped implanted markers in kilovoltage projection images: A feasibility study. *Medical Physics*, 41(7):071906, 2014.

[42] P. R. Poulsen, B. Cho, and P. J. Keall. A method to estimate mean position, motion magnitude, motion correlation, and trajectory of a tumor from cone-beam ct projections for image-guided radiotherapy. *International Journal of Radiation Oncology, Biology, Physics*, 72(5):1587–1596, 2008.

[43] E. S. Worm, M. Høyer, W. Fledelius, J. E. Nielsen, L. P. Larsen, and P. R. Poulsen. On-line use of three-dimensional marker trajectory estimation from cone-beam computed tomography projections for precise setup in radiotherapy for targets with respiratory motion. *International Journal of Radiation Oncology, Biology, Physics*, 83(1):e145–e151, 2012.

[44] J. Ge, L. Santanam, D. Yang, and P. J. Parikh. Accuracy and consistency of respiratory gating in abdominal cancer patients. *International Journal of Radiation Oncology, Biology, Physics*, 85(3):854 – 861, 2013.

[45] H. Wan, P. Parikh, D. Muccigrosso, R. Bera, H. Shultejans, A. Curcuru, L. Santanam, and R. Pless. Tumor tracking in low-field cine-mr images. *Medical Image Computing and Computer-Assisted Intervention – MICCAI 2016*, 2016.

[46] A. J. Lipton, H. Fujiyoshi, and R. S. Patil. Moving target classification and tracking from real-time video. In *Applications of Computer Vision, 1998. WACV'98. Proceedings., Fourth IEEE Workshop on*, pages 8–14. IEEE, 1998.

[47] C. Stauffer and W. E. L. Grimson. Adaptive background mixture models for real-time tracking. In *Computer Vision and Pattern Recognition, 1999. IEEE Computer Society Conference on.*, volume 2. IEEE, 1999.

[48] D. Comaniciu, V. Ramesh, and P. Meer. Real-time tracking of non-rigid objects using mean shift. In *Computer Vision and Pattern Recognition, 2000. Proceedings. IEEE Conference on*, volume 2, pages 142–149. IEEE, 2000.

[49] Y. Shi and W. C. Karl. Real-time tracking using level sets. In *Computer Vision and Pattern Recognition, 2005. CVPR 2005. IEEE Computer Society Conference on*, volume 2, pages 34–41. IEEE, 2005.

[50] B. K. Horn and B. G. Schunck. Determining optical flow. In *1981 Technical symposium east*, pages 319–331. International Society for Optics and Photonics, 1981.

[51] T. R. Mazur, B. W. Fischer-Valuck, Y. Wang, D. Yang, S. Mutic, and H. H. Li. Sift-based dense pixel tracking on 0.35 t cine-mr images acquired during image-guided radiation therapy with application to gating optimization. *Medical Physics*, 43(1):279–293, 2016.

[52] Q. Zhang, A. Pevsner, A. Hertanto, Y.-C. Hu, K. E. Rosenzweig, C. C. Ling, and G. S. Mageras. A patient-specific respiratory model of anatomical motion for radiation treatment planning. *Medical Physics*, 34(12):4772–4781, 2007.

[53] R. Li, J. H. Lewis, X. Jia, T. Zhao, W. Liu, S. Wuenschel, J. Lamb, D. Yang, D. A. Low, and S. B. Jiang. On a pca-based lung motion model. *Physics in Medicine and Biology*, 56(18):6009, 2011.

[54] S. Lankton and A. Tannenbaum. Localizing region-based active contours. *Image Processing, IEEE Transactions on*, 17(11):2029–2039, 2008.

[55] A. Yezzi, A. Tsai, and A. Willsky. A fully global approach to image segmentation via coupled curve evolution equations. *Journal of Visual Communication and Image Representation*, 13(1):195–216, 2002.

[56] M.-P. Dubuisson and A. K. Jain. A modified hausdorff distance for object matching. In *Pattern Recognition, 1994. Vol. 1-Conference A: Computer Vision & Image Processing., Proceedings of the 12th IAPR International Conference on*, volume 1, pages 566–568. IEEE, 1994.

Curriculum Vitae

Hanlin Wan

Degrees

Ph.D. Biomedical Engineering
Washington University, St. Louis, MO
May 2016

B.S. Biomedical Engineering
B.S. Computer Engineering
Johns Hopkins University, Baltimore, MD
May 2011

Professional Societies and Awards

American Association of Physicists in Medicine
American Society for Therapeutic Radiation Oncology
Reviewer - International Journal of Radiation Oncology, Biology, Physics

Patents

P. Parikh, **H. Wan**. Template-less method for arbitrary radiopaque object tracking in dynamic imaging. U.S. Patent Application No. 20,150,254,859. 2015.

Publications

H. Wan, P. Parikh, D. Muccigrosso, R. Bera, H. Shultejans, A. Curcuru, L. Santanam, and R. Pless. Tumor tracking in low-field cine-MR images. *Medical Image Computing and Computer-Assisted Intervention – MICCAI 2016*, In submission.

H. Wan, J. Bertholet, J. Ge, P. Poulsen, and P. Parikh. Automated patient setup and gating using cone beam computed tomography projections. *Physics in Medicine and Biology*, 61(6):2552, 2016.

L. Rankine, **H. Wan**, P. Parikh, N. Maughan, P. Poulsen, T. DeWees, E. Klein, and L. Santanam. Cone-beam computed tomography internal motion tracking should be used to validate 4-dimensional CT for abdominal radiotherapy patients. *International Journal of Radiation Oncology, Biology, Physics*, 2016. In press.

H. Wan, J. Ge, and P. Parikh. Using dynamic programming to improve fiducial marker localization. *Physics in Medicine and Biology*, 59(8):1935, 2014.

M. Nasiriavanaki, J. Xia, **H. Wan**, A.Q. Bauer, J.P. Culver, and L.V. Wang. High-resolution photoacoustic resting-state functional connectivity imaging of the mouse brain. *Proceedings of the National Academy of Sciences*, 111(1):21-26, 2014.

A.T. Dennis, L.Wang, **H. Wan**, D. Nassal, I. Deschenes, and E. Ficker. Molecular determinants of pentamidine-induced herg tracking inhibition. *Molecular Pharmacology*, 81(2):198-209, 2012.

B.A. Landman, J.A. Bogovic, **H. Wan**, F.E.Z. ElShahaby, P.L. Bazin, and J.L. Prince. Resolution of crossing fibers with constrained compressed sensing using diffusion tensor MRI. *NeuroImage*, 59(3): 2175-2186, 2012.

Selected Proceedings

H. Wan, J. Bertholet, *et al*. Automated gating patient setup with CBCT fiducial marker tracking. *EPI*, 2016.

Jenny Bertholet, **H. Wan**, *et al*. Fully automatic segmentation of arbitrarily shaped fiducial markers in CBCT projections. *ICCR*, 2016.

Y. Lu, I. Chen, R. Kashani, **H. Wan**, *et al*. Interactive auto-segmentation for bowel in online adaptive MRI-guided radiation therapy by using a multi-regional labeling algorithm. *AAPM*, 2016.

K. Grantham, **H. Wan**, *et al*. Stability of mean lung tumor position over the courses of radiation therapy as measured by continuous electromagnetic transponder tracking. *ASTRO*, 2016.

D. Muccigrosso, N. Maughan, **H. Wan**, *et al*. The relationship between implantation distance and fraction number with fiducial accuracy during lung cancer radiation therapy. *ASTRO*, 2016.

H. Wan, P. Poulsen, *et al*. A fully automated motion assessment and gated patient setup in radiation therapy. *ASTRO*, 2015.

L. Rankine, **H. Wan**, *et al*. CBCT measures abdominal tumor motion better than 4DCT and equal to on-table fluoroscopy. *ASTRO*, 2015.

B. W. Fischer-Valuck, T. R. Mazur, S. Acharya, **H. Wan**, *et al*. Accelerated partial-breast irradiation utilizing an on-board magnetic resonance image guided radiation therapy system. *ASTRO*, 2015.

L. Santanam, C. Noel, **H. Wan**, *et al*. Adequacy of gating margins for abdominal tumors of patients treated with real-time MR-guided RT. *ASTRO*, 2015.

H. Wan, R. Pless, *et al*. Real-time tumor motion tracking in low field cine-MR images. *AAPM*, 2015.

H. Wan, R. Pless, *et al*. Real-time tumor motion tracking in low field cine-MR images using principal component analysis. *MR in RT*, 2015.

H. Wan, J. Ge, *et al*. Fiducial marker motion tracking using dynamic programming. *AAPM*, 2012.

B. A. Landman, **H. Wan**, *et al*. Resolution of crossing fibers with constrained compressed sensing using traditional diffusion tensor MRI, *SPIE Medical Imaging*, 2010.

B.A. Landman, **H. Wan**, *et al*. In the pursuit of intra-voxel fiber orientations: comparison of compressed sensing DTI and Q-Ball MRI, *ISMRM*, 2010.

B. A. Landman, **H. Wan**, *et al*. Accelerated compressed sensing of diffusion-inferred intra-voxel structure through adaptive refinement, *ISMRM*, 2010.